

Development of Water Čerenkov Detector for On-line Proton Rejection in Ξ^- Hypernuclear Spectroscopy via the (K^-, K^+) Reaction

T. Gogami, N. Amamo, S. Kanatsuki,
T. Nagae and K. Takenaka

*Department of Physics, Graduate School of Science,
Kyoto University, Kyoto, 606-8502, Japan*

Abstract

A missing mass spectroscopy of Ξ^- hypernuclei with the (K^-, K^+) reaction is planned to be performed at J-PARC K1.8 beam line using a new magnetic spectrometer, S-2S. A Čerenkov detector with a radiation medium of pure water (refractive index of 1.33) is designed to be used for on-line proton rejection for a momentum range from 1.2 to 1.6 GeV/ c in S-2S. Prototype water Čerenkov detectors were developed and tested with positron beams and cosmic-rays to estimate their proton rejection powers. The latest prototype was able to achieve NPE > 200 for a cosmic-ray with a sufficient stability during an expected beam time. As a result of a Monte Carlo simulation with inputs from the cosmic-ray test, the prototype water Čerenkov detector is expected to achieve $> 90\%$ proton rejection efficiency keeping $> 95\%$ K^+ survival ratio in the whole S-2S acceptance. The performance fulfills our requirements to carry out the spectroscopic experiment of Ξ^- hypernuclei at J-PARC.

1 Introduction

A spectroscopic experiment of Ξ^- hypernucleus by the (K^-, K^+) reaction is planned to be performed at J-PARC (J-PARC E05) [1]. The experiment is the first attempt to measure Ξ^- hypernucleus with a few MeV energy resolution

(FWHM) using a new magnetic spectrometer, S-2S (Strangeness -2 Spectrometer). S-2S was designed to measure K^+ momentum with a resolution of $\Delta p/p \simeq 5.0 \times 10^{-4}$ in FWHM. Expected major background particles are protons and π^+ s. According to a Monte Carlo simulation, about a thousand times higher rates of protons and π^+ s relative to K^+ s are expected in S-2S. Therefore, a background suppression at a trigger level (on-line) is essential to carry out the experiment in a given beam time, keeping sustainable rates for a Data AcQuisition system (DAQ).

The background particle suppression with Čerenkov detectors was well established in the past Λ hypernuclear experiments [2, 3, 4]. In the J-PARC E05 experiment, the background particle suppression is also designed to be done with Čerenkov detectors. However, they should be dedicated to the new magnetic spectrometer system, S-2S. π^+ s will be rejected by existing aerogel (refractive index of 1.05) Čerenkov detector which was used in Λ hypernuclear experiments with Superconducting Kaon Spectrometer (SKS). On the other hand, a Čerenkov detector suppressing protons in the S-2S momentum and geometrical acceptances does not exist. In the present article, development and performance test of prototype Čerenkov detectors with radiation medium of pure water (refractive index of 1.33) for the proton suppression in S-2S are described.

2 Requirements for Water Čerenkov Detector

Fig. 1 shows a schematic drawing of S-2S top view. S-2S consists of drift chambers for particle tracking, Time Of Flight (TOF) detector for trigger and off-line Particle IDentification (PID), and Čerenkov detectors for on-line PID. A water Čerenkov detector is planned to be installed at the most downstream of particle detectors. The water Čerenkov detector is designed to be segmented by six per a layer taking into account its handling and performance of each segment. To avoid inefficient region, another layer is planned to be installed after the first layer with an offset by a half-segment (Fig. 1 and Fig. 35). Thus, twelve segments in total will be installed.

S-2S measures momenta of particles with a range from 1.2 to 1.6 GeV/ c . Fig. 2 shows the photon yield of Čerenkov light per cm in water as a function

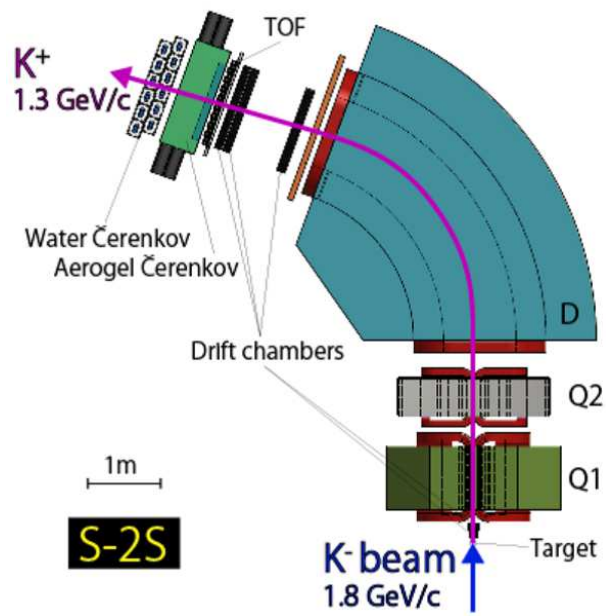


Figure 1: A schematic drawing of the experimental setup of J-PARC E05 experiment.

of an incident particle (π^+ , K^+ , p) momentum calculated by the following [5]:

$$\frac{d^2N}{dx d\lambda} = \frac{2\pi\alpha z^2}{\lambda^2} \left(1 - \frac{1}{\beta^2 n^2(\lambda)}\right) \quad (1)$$

where N and λ are the number of photons and wavelength of Čerenkov light, x , z and β are the path length, charge and velocity factor of incident particle, $n(\lambda)$ is the refractive index of radiation medium. In Fig. 2, the wavelength was integrated from 300 nm to 600 nm which corresponds to a rough sensitive region of photo multiplier tube (PMT), and $n(\lambda)$ is fixed at 1.33 which is the nominal refractive index of pure water. All three particles yield Čerenkov light in water in the S-2S momentum acceptance, but can be identified by a difference of photon yield. Protons are planed to be suppressed at a trigger level (on-line) by a photon yield cut in the water Čerenkov detector.

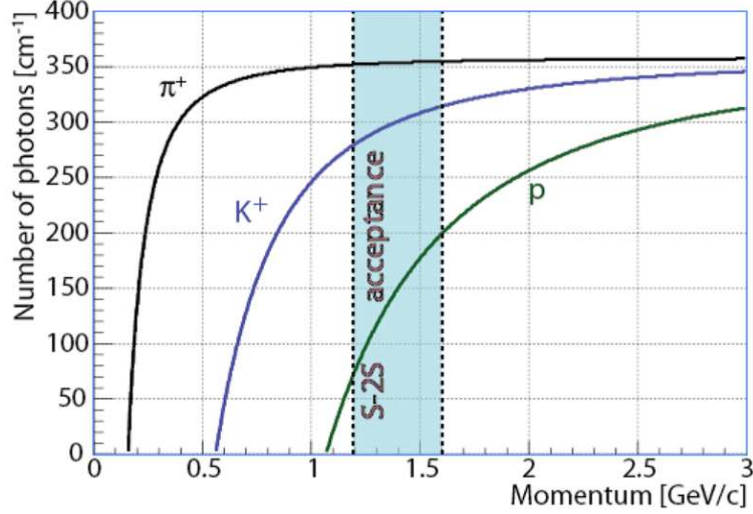


Figure 2: The photon yield of Čerenkov light per cm in water ($n = 1.33$) as a function of incident particle (π^+ , K^+ , proton) momentum calculated by Eq. (1).

A Čerenkov light is converted to electrons (photoelectrons) and multiplied by PMT to be detected as signals. Photon yield which is measured as the number of photoelectrons (NPE) depends on a container shape of radiation medium, window material used between the radiation medium and PMT,

reflection material of the container inside, and PMT performance *etc.* Top figure in Fig. 3 shows expected NPE histograms with simple Poisson distributions for proton and K^+ with momenta of 1.3 GeV/ c , assuming the mean values for 1.3 GeV/ c K^+ are 25 (dashed line, $N_K = 25$) and 50 (solid line, $N_K = 50$). In the bottom two figures in Fig. 3, survival ratios of protons and K^+ s as a function of cut threshold are shown. If one chooses a cut threshold rejecting 99% of protons, the survival ratios of K^+ s for $N_K = 25$ and $N_K = 50$ are respectively 92.7% and 99.8%. As describe above, higher K^+

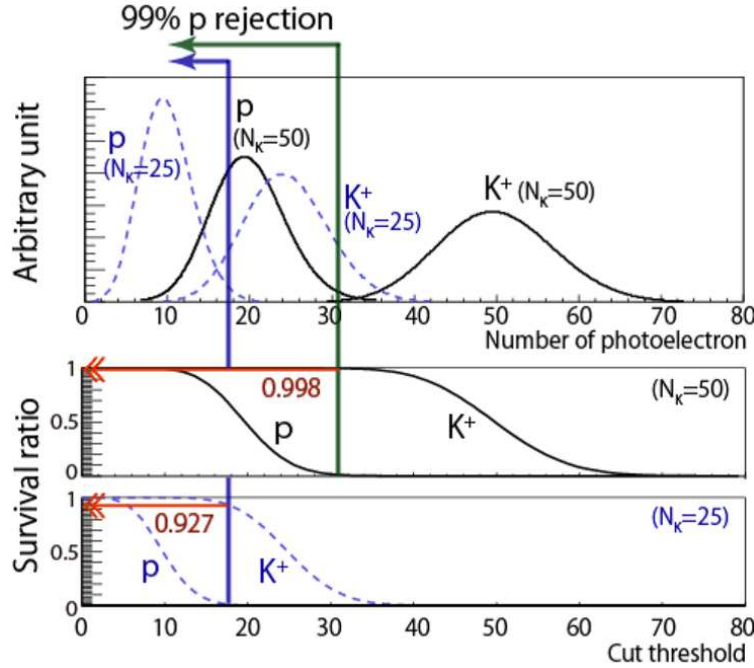


Figure 3: Top figure shows the expected distribution (Poisson distribution) of the number of photoelectrons for protons and K^+ s with momenta of 1.3 GeV/ c , assuming the mean values for 1.3 GeV/ c K^+ are 25 (dashed line, $N_K = 25$) and 50 (solid line, $N_K = 50$). Bottom two figures show survival ratios of protons and K^+ s as a function of cut threshold. If one chooses a cut threshold rejecting 99% of protons, the survival ratios of K^+ for $N_K = 25$ and $N_K = 50$ are respectively 92.7% and 99.8%.

survival ratio can be achieved by a detector that has a larger NPE detection power when the proton rejection efficiency is fixed.

In the J-PARC E05 experiment, 10^6 counts/spill K^- beam^{*1} is planned to be used at K1.8 beam line in J-PARC. Counting rates of protons, K^+ s and π^+ s from a 3 g/cm² ¹²C target are estimated to be 150, 1 and 20 [counts/ 10^6 K^- beams], respectively by using a Monte Carlo simulation (Geant4 [6]). Background particles which do not originate from the target such as decayed particles from K^- beams is also simulated by the Monte Carlo method, and the counting rate is expected to be a few 10 [counts/ 10^6 K^- beams]. It is considered that the rate estimation is not far from the reality in S-2S as the Monte Carlo simulation is able to reproduce particle rates (proton, π^+ and γ) in a test experiment using SKS spectrometer with K^- beams at J-PARC in 2015. A safety factor of five was multiplied to the estimated background counting rate ($\sim 200 \times 5 = 1000$ [counts / 10^6 K^- beams]) , and the value was used for a S-2S detector design. A DAQ rate would be better to be below a few hundreds counts/spill in order to take data with a sufficient efficiency. The existing aerogel Čerenkov detector is able to reject $> 99.7\%$ of π^+ s with $\sim 93\%$ of K^+ survival ratio at the trigger level [7, 8]. Therefore, $\geq 90\%$ of proton rejection efficiency keeping $\geq 95\%$ of K^+ survival is aimed by a water Čerenkov detector at the trigger level.

3 Prototype Water Čerenkov Detector

A prototype water Čerenkov detector was constructed and tested by irradiating positron beams at ELPH. In this section, the prototype design and results of the beam test are described.

3.1 Design of the Prototype Water Čerenkov Detector

A prototype water Čerenkov detector consists of a white acrylic container with transparent acrylic windows faced by PMT photocathodes, PMTs and pure water. The container was made of 15 mm thickness white acrylic boards which were bond by polymerization bonding except for a cap part. The cap part and the main container was attached by winding with polypropylene band (PP band). A diffuse reflection material attached on the container's inside was chosen to be Tyvek sheet (Tyvek 1060B^{*2}) which is widely used for building material. PMTs (Hamamatsu H11284-100UV [16]) were attached on

^{*1}Two seconds of flat top is expected at the moment.

^{*2}DuPont, <http://www.dupont.com/>

the top and bottom of the container using a silicon optical coupling grease (BC-630^{*3}, $n = 1.465$). In between the radiation medium and the PMT, 5 mm thickness windows made of transparent acrylics (Acrylite#001^{*4}) were attached. Fig. 4 shows a drawing of a prototype water Čerenkov detector. The effective volume was $200^w \times 700^h \times 150^t$ mm³.

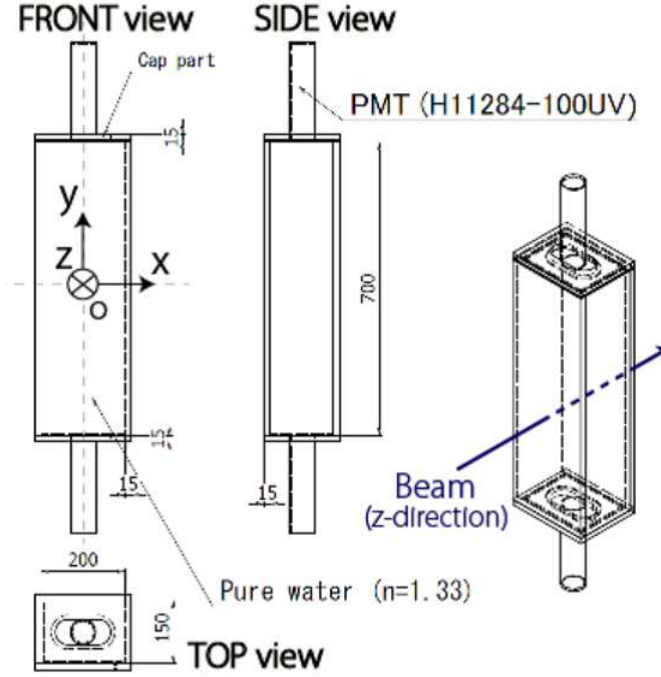


Figure 4: A drawing of the prototype water Čerenkov detector. x , y and z coordinates are defined in the drawing. The unit is mm.

3.2 Experimental setup

A test experiment was performed using positron beams in positron/electron beam line at Research Center for Electron Photon Science, Tohoku University (ELPH) [9, 10] in order to investigate basic performance of the prototype water Čerenkov detector such as position and angular dependencies of NPE.

^{*3}Saint-Gobain Crystals, <https://www.saint-gobain.com/fr>

^{*4}Mitsubishi Rayon company, <http://www.mrc.co.jp/acrylite/>

Fig. 5 shows a schematic drawing of the experimental setup. Positron

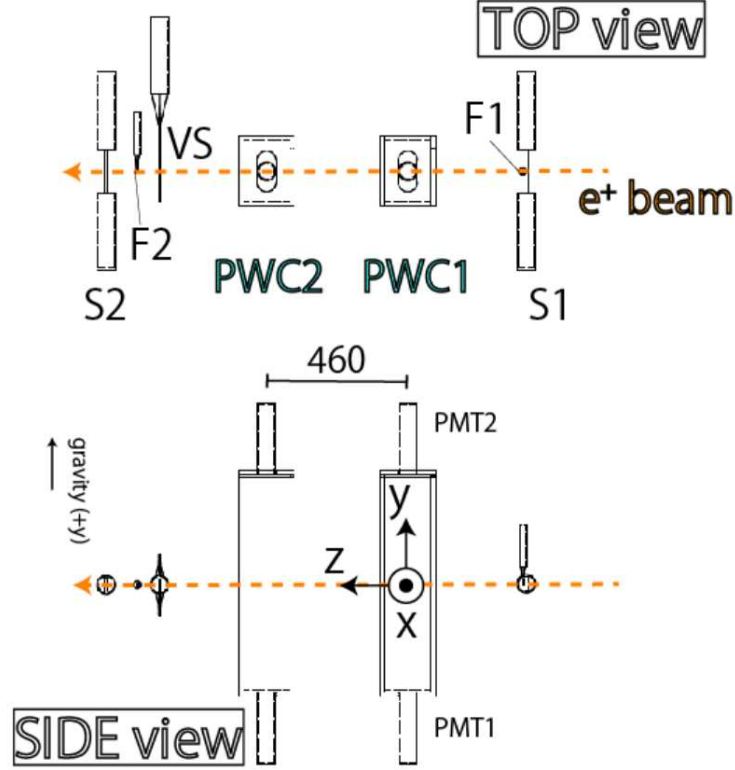


Figure 5: A schematic drawing of experimental setup at ELPH. Positron beams with $\beta = 1$ were incident on two sets of prototype water Čerenkov detectors (PWC). The unit in the figure is mm.

beams with $\beta = 1$ ($\beta > 0.99999$) were impinged on two sets of prototype water Čerenkov detectors (PWC1, PWC2). Two plastic scintillation detectors (S1, F1) before PWCs, and three plastic scintillation detectors (VS, F2, S2) after PWCs were installed. VS had a $\phi 25$ mm hole at the center so as to be used as an off-line veto for background particles. S1, S2 and F1 were used for both data taking trigger and off-line analysis. Detector sizes and distances with respect to S1 are summarized in Table 1.

PWCs could be displaced and tilted using a movable frame in order to change incident positions and angles of beams on PWCs. x - and y -coordinates are defined in Fig. 5, and x' and y' are the angles of incident

Table 1: Sizes and distances from S1 in beam direction of detectors used in the test experiment at ELPH.

Detector	Distance [mm]	Size [mm]	Remarks
S1	0	$144^W \times 44^H \times 10^T$	Filled with pure water Filled with pure water A $\phi 25$ hole at the center
F1	6	$9.3^W \times 9.3^H \times 4^T$	
PWC1	382	$200^W \times 700^H \times 150^T$	
PWC2	842	$200^W \times 700^H \times 150^T$	
VS	1190	$200^W \times 200^H \times 5^T$	
F2	1266	$9.8^W \times 9.5^H \times 4^T$	
S2	1369	$144^W \times 10^H \times 0^T$	

beams on PWC.

3.3 Analysis

3.3.1 NPE calibration

Charge information from each PMT of the water Čerenkov detector was obtained by Analog to Digital Converter (ADC). The ADC was then converted to NPE using data of NPE measurements with an LED light (Para Light LED 3.0 mm L-314LBD^{*5}) which was installed in the container of water Čerenkov detector. The LED light intensity was adjusted to be a few NPE detection on each PMT by controlling height and width of input rectangular pulses generated by an Arbitrary/Function generator. Fig. 6 shows an ADC histogram of H11284-100UV using the LED light. The ADC histogram was fitted by a convoluted function of Gaussian function for pedestal, Poisson functions for photoelectron peaks and an exponential function for residual background events between the pedestal and a single photoelectron peak (1 p.e.) [11]. ADC channels per a single photoelectron was then obtained by the fitting result, which was used for a conversion from an ADC histogram to an NPE histogram.

^{*5}Para Light Electronics company, <http://www.para.com.tw/>

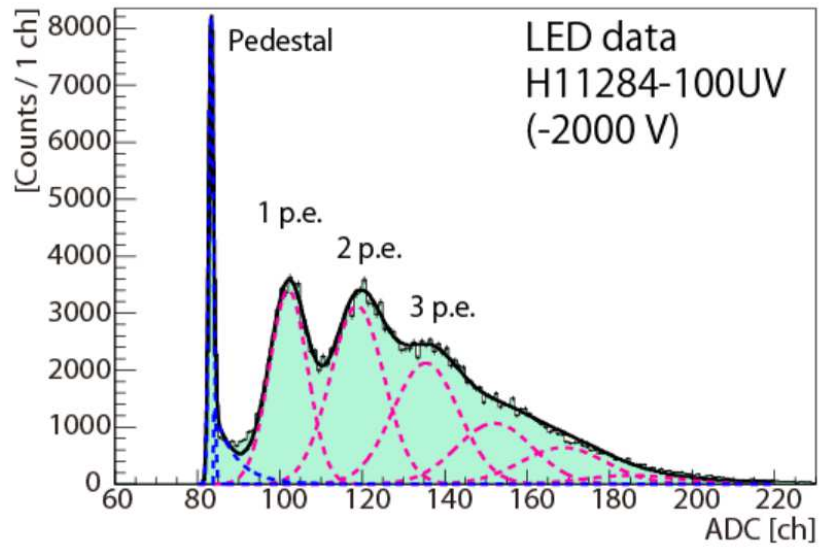


Figure 6: An ADC histogram of H11284-100UV using LED. The ADC histogram was fitted by a convoluted function of Gaussian function for pedestal, Poisson functions for photoelectron peaks and exponential function for residual background events between the pedestal and a single photoelectron peak (1 p.e.) [11].

3.3.2 NPE Derivation

The NPE histograms were fitted with Gaussian functions, and the mean values were used as results. An event select condition was applied for the NPE analysis as the following:

$$S1 \otimes S2 \otimes F1 \otimes F2 \otimes \overline{VS}, \quad (2)$$

where S1, S2, F1, F2 and VS correspond to ADC and TDC selections for each detector. In addition, TDC^{*6} selections of PWCs were also applied to select events in an appropriate timing. Fig. 7 shows a typical NPE histogram with a fitting result after the above event selections were applied.

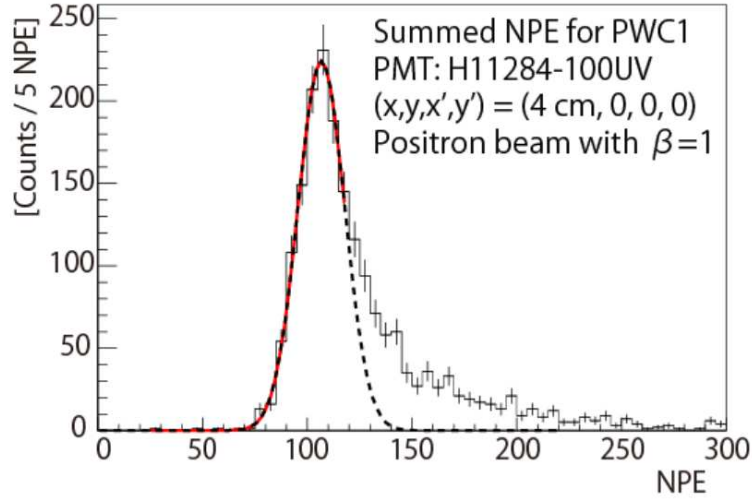


Figure 7: A typical NPE histogram with a fitting result after the event selection of Eq.(2) and PWC TDC selection were applied. The mean value obtained by the fitting was used as a result.

3.4 Results

3.4.1 NPE at Center position

Obtained NPEs for PWC1 and PWC2 at $(x, y, x', y') = (0, 0, 0, 0)$ were summarized in Table. 2. The NPE detected by each PMT was about 65 except

^{*6}Time to Digital Converter

Table 2: NPEs for PWC1 and PWC2 when positron beams were impinged at $(x, y, x', y') = (0, 0, 0, 0)$. Errors on the results are statistical.

	PWC1	PWC2
PMT1 (top)	64.8 ± 0.3	65.2 ± 1.0
PMT2 (bottom)	41.2 ± 0.2	65.6 ± 1.9
Sum	105.7 ± 0.4	135.0 ± 0.8

for the bottom PMT of PWC1 (PWC1-2). The smaller NPE of PWC1-2 could be caused by an air gap between the PMT and acrylic window. As shown Sec. 5.2.8, an air gap causes about 35% reduction of NPE. If the NPE of PWC1-2 is corrected by a factor of $f_{\text{gap}} = \frac{1}{(1.00-0.35)}$, the NPE becomes $\text{NPE}_{f_{\text{gap}}}^{\text{PMT1-2}} = 63.4 \pm 0.3$ which is then consistent with the others within the standard deviation of PMT individual performance difference ($\sigma_{\text{PMT}} = 6\%$, Sec. 5.2.6). The air gap was considered to be caused by a loose PMT fixing by the frame.

3.4.2 y' Dependence

Summed NPEs (sum of top and bottom PMTs) of PWC1 were obtained to be:

$$\text{NPE}_{\text{center}}^{y'=0^\circ} = 135.0 \pm 0.8, \quad (3)$$

$$\text{NPE}_{\text{center}}^{y'=8^\circ} = 84.3 \pm 0.5 \quad (4)$$

at $(x, y, x', y') = (0, 0, 0, 0)$ and $(0, 0, 0, 8^\circ)$, respectively. There was a large NPE reduction in $\text{NPE}_{\text{center}}^{y'=8^\circ}$ compared to $\text{NPE}_{\text{center}}^{y'=0^\circ}$. The NPE reduction would be caused by detachment of PMTs from acrylic windows when the PWC was tilted to see the angular dependence as well as the situation of PWC1-2 in Sec. 3.4.1. If the $\text{NPE}_{\text{center}}^{y'=8^\circ}$ is corrected by f_{gap} :

$$\text{NPE}_{\text{center}}^{y'=8^\circ} \times f_{\text{gap}} = 130.0 \pm 0.8. \quad (5)$$

The NPE variation was obtained to be about 4% in the range of $y' = 0 \sim 8$ deg by comparing Eq. (3) and Eq. (5).

3.4.3 y -position Dependence

Fig. 8 shows a y -position dependence of NPE at $(x, x') = (0, 0)$ for $y' = 0$ and 8 deg. The NPE values were normalized so as to make the NPEs at $(x, x', y) = (0, 0, 0)$ unity.

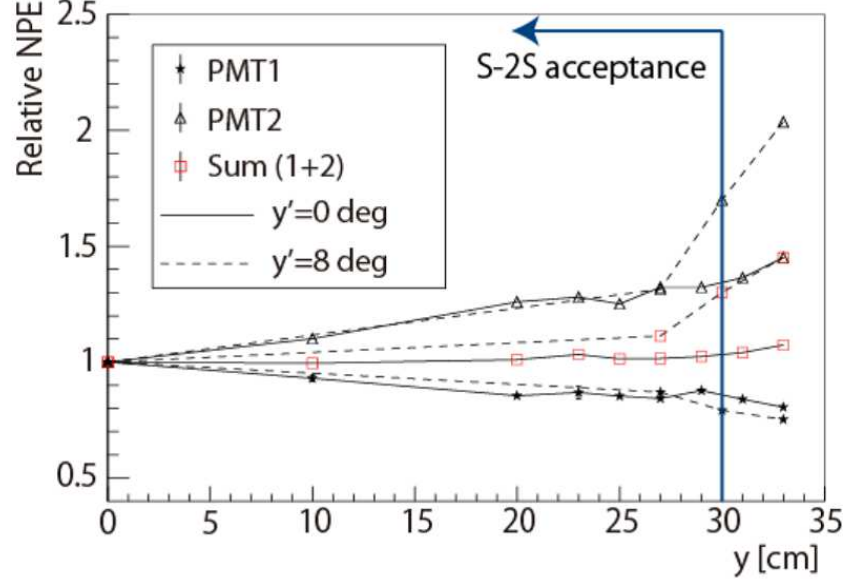


Figure 8: Relative NPEs as a function of y for $y' = 0$ and 8 deg.

The NPE of PMT2 for $y' = 8$ deg was steeply increased at around $y = 28$ cm. This is considered to be caused by a direct Čerenkov light detection on the PMT. The Čerenkov radiation angle relative to an incident particle direction is calculated as the following [5]:

$$\theta_C = \arctan(\sqrt{\beta^2 n^2 - 1}) \quad (6)$$

Thus, the radiation angle of a $\beta = 1$ particle in water ($n = 1.33$) is obtained to be:

$$\theta_C^{\beta=1} = 41.2^\circ. \quad (7)$$

Taking into account the radiation angle, the geometry of the prototype water Čerenkov detector and the refraction between water and acrylic window ($n =$

1.49), the direct Čerenkov light arrival on the PMT photocathode occurs at $y = 24$ cm and $y = 27$ cm for $y' = 0$ and 8 deg, respectively. In the results, however, the NPE rising starts at around $y = 28$ cm for $y' = 8$ deg. The difference would be due to the air gap between the optical coupling grease and PMT. Moreover, there is no such rising for $y' = 0$ deg. This could be also caused by the air gap. A Čerenkov light directly reaches the PMT photocathode if there is no air gap as shown in the left schematic diagram of Fig. 9. On the other hand, a Čerenkov light that satisfies the following condition does not reach the PMT photocathode directly due to the total reflection at a boundary between the air and optical coupling grease:

$$\theta_{\text{in}} \geq 90^\circ - \arcsin\left(\frac{n_2}{n_1}\right) = 41.2^\circ \quad (8)$$

where θ_{in} ($0^\circ \leq \theta_{\text{in}} < 90^\circ$) is the angle of light with respect to the z -axis in yz -plane, n_1 and n_2 are respectively the refractive indexes of water ($n = 1.33$) and air ($n = 1.00$). In the calculation, it is assumed that the thickness of the optical grease is zero. Using Eq. (7), θ_{in} for $y' = 0$ deg and $y' = 8$ deg are obtained to be:

$$\theta_{\text{in}}^{y'=0^\circ} = \theta_C^{\beta=1} - 0^\circ = 41.2^\circ, \quad (9)$$

$$\theta_{\text{in}}^{y'=8^\circ} = \theta_C^{\beta=1} - 8^\circ = 33.2^\circ. \quad (10)$$

According to Eq. (8), Eq. (9) and Eq. (10), the total reflection occurs for $y' = 0$ deg, but does not for $y' = 8$ deg as shown in a right schematic diagram in Fig. 9, which is consistent with what we observed in Fig. 8.

In the S-2S experiment, the proton rejection efficiency would be reduced if the direct Čerenkov light detection is happened, keeping the same K^+ detection efficiency. Fig. 10 shows a y threshold of the direct Čerenkov light arrivals on a PMT photocathode as a function of proton momentum for $y' = 0$ and 8 deg. The y thresholds for particles with $\beta = 1$ are also shown for references. The S-2S acceptance is shown as a colored box, and the thresholds of protons are barely in the acceptance. However, the ratio of the number of events which would cause the direct Čerenkov light detection to those in the whole S-2S acceptance is estimated to be $< 0.1\%$ according to a Monte Carlo simulation. Therefore, an effect of the proton rejection efficiency reduction due to the direct Čerenkov light detection is considered to be negligible small.

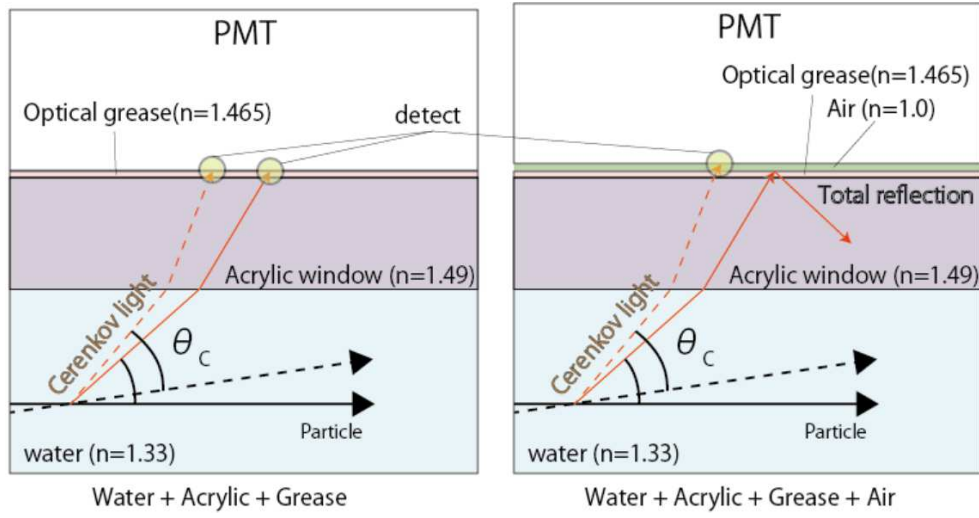


Figure 9: A schematic diagrams for the direct Čerenkov light detection by PMT. The total reflection is occurred for $y' = 0$ deg before the PMT photocathode if there is an air gap between the optical coupling grease and PMT as described in the right figure.

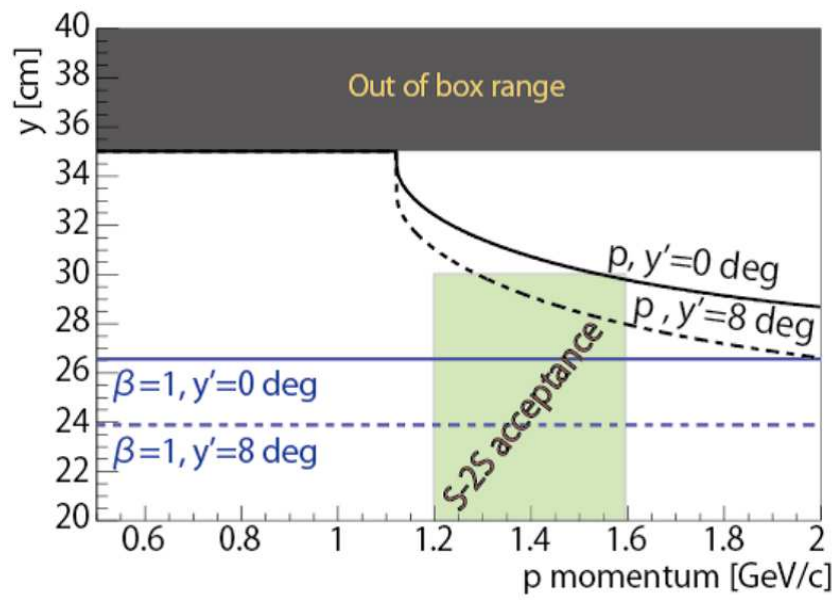


Figure 10: Calculated thresholds to detect direct Čerenkov light on PMT in the prototype water Čerenkov detector for incident particles with $y' = 0$ and 8 deg.

3.4.4 x, y -position Dependence

Fig. 11 shows a summed NPE histogram in two-dimensions for $(x', y') = (0, 0)$. The NPE at $(x, y) = (0, 0)$ is normalized to be unity in the figure. It was found that the NPE is higher for larger $|y|$, and lower for larger $|x|$. The NPE variation depending on the incident beam position was measured to be $< \pm 10\%$.

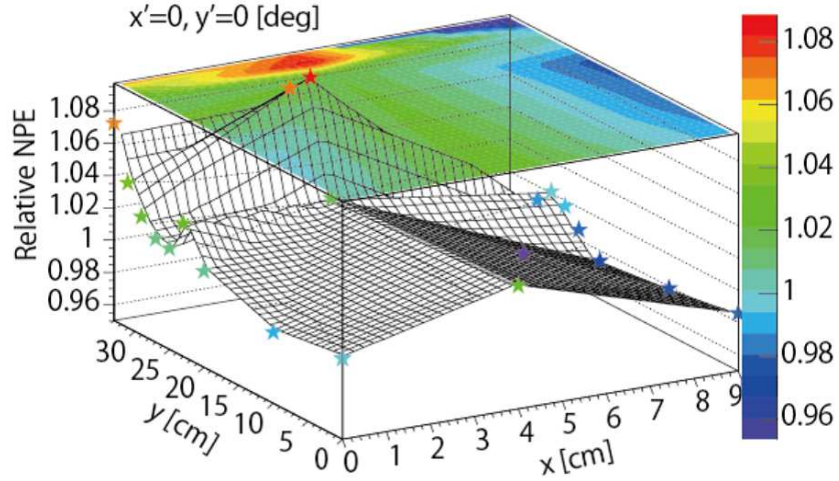


Figure 11: A dependence of the normalized NPE on x and y detected by the prototype water Čerenkov detector at $(x', y') = (0, 0)$.

3.4.5 x' Dependence

The horizontal beam angle, x' was also varied in the beam test ($x' \leq 8$ deg), but no dependence on x' was observed within the error after a path length correction.

3.4.6 Summary of the beam test

In summary of the $\beta = 1$ positron beam test, the prototype water Čerenkov detector was able to achieve a summed NPE of ≥ 130 for a $\beta = 1$ particle. An NPE variation of $< 10\%$ due to the beam position and angular dependencies are expected for almost all particles in the S-2S acceptance.

4 Window Material Optimization

A Monte Carlo simulation which took into account the NPE detection power of the previous prototype water Čerenkov detector was performed in order to estimate the proton rejection efficiency. The Monte Carlo simulation showed that the proton rejection efficiency at higher momentum region in S-2S would not be enough. Therefore, the NPE detection power was tried to be improved by optimizing a choice of window material. Motivation and a cosmic-ray test of the window material optimization are described in this section.

4.1 Motivation

The prototype water Čerenkov detector (PWC) was able to achieve $\text{NPE} \geq 130$ (sum of top and bottom PMTs) for a $\beta = 1$ particle as shown in the previous section. A Monte Carlo simulation which took into account the obtained NPE was done to estimate a proton rejection efficiency with the same framework as shown in Sec.6. Fig. 12 shows estimated survival ratios for protons and K^+ s as a function of particle momenta in S-2S assuming that $\text{NPE} = 120^{*7}$ for $\beta = 1$ particles. The proton rejection efficiency at around 1.6 GeV/c is smaller than the our goal of 90% keeping the K^+ survival ratio of $\geq 95\%$. Thus, a further development to improve NPE was needed.

4.2 Window Material Effect on NPE

Fig. 13 shows the calculated number of photons of Čerenkov light per unit length of incident particle per wavelength as a function of the wavelength for proton, K^+ and π^+ with momenta of 1.3 GeV/c (Eq. (1)). As shown in the figure, Čerenkov light of shorter wavelength yields more photons since the number of photons is in inverse proportion to the wavelength. Therefore, it is a key point to avoid light absorption particularly for ultraviolet light as small as possible in order to achieve larger NPE detection power. A light yield loss is mainly occurred by water, acrylic window, optical coupling grease and PMT window glass. A quantum efficiency of PMT should also be considered as it is related to a detection of a Čerenkov light as an electric signal.

^{*7}Assumed smaller NPE value by about 10% compared to that obtained in the positron beam test.

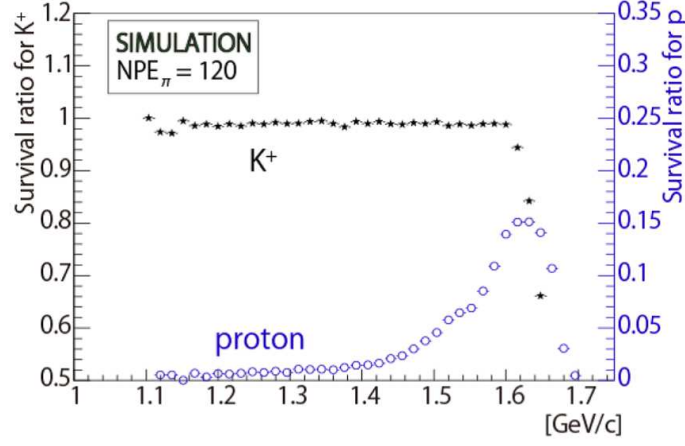


Figure 12: The estimated survival ratios for protons and K^+ s in S-2S as a function of particle momenta at the particle generation point, assuming $NPE=120$ for $\beta = 1$ particles.

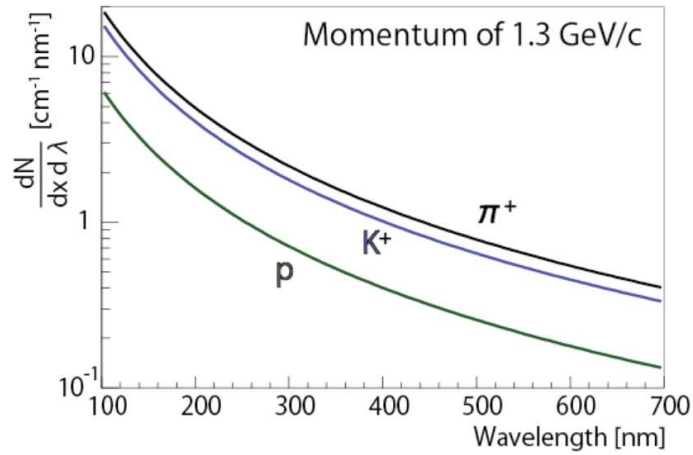


Figure 13: Number of photons of Čerenkov light per unit path length of incident particle per wavelength as a function the wavelength for proton, K^+ and π^+ with momenta of 1.3 GeV/c.

Light Absorption by Water Absorption spectra of water are shown in Fig. 14. In the figure, three experimental data were plotted. One is taken from [12], and is labeled as “Experimental data 1”. The others are taken from [13] and [14] with covered ranges of 200 nm \sim 320 nm and 380 nm \sim 700 nm, respectively. These two data are labeled as “Experimental data 2”. Dashed lines represent extrapolations and an interpolation of the experimental data. The absorption coefficients especially for UV region are different between

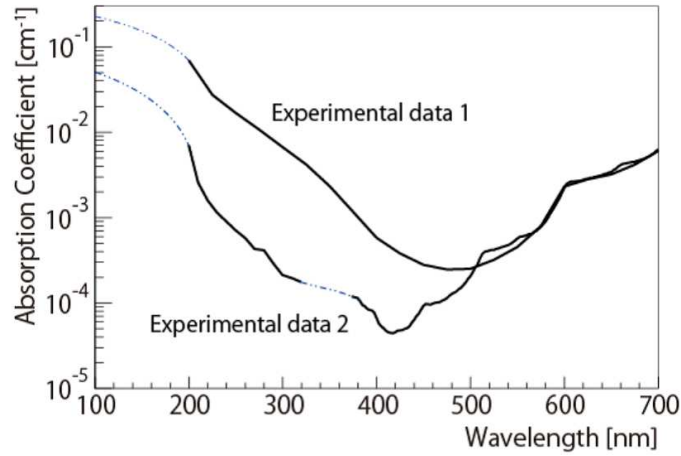


Figure 14: Absorption spectrum of water. Experimental data were taken from [12, 13, 14]. Dashed lines represent extrapolations and an interpolation of the experimental data.

“Experimental data 1” and “Experimental data 2”. The difference is caused by a difference of water purity, and purer water has a smaller absorption coefficient for UV region [14]. Thus, water should be pure as much as possible for the use of water Čerenkov detector, and a handling of water has to be careful not to make it dirty.

Transmittance of Acrylic Window Fig. 15 shows measured transmittance of the following acrylic materials with thicknesses of 5 mm:

- Acrylite#001
- Acrylite#000*⁸

*⁸Mitsubishi Rayon company, <https://www.mrc.co.jp/>

- UV00^{*9}
- S-0^{*10}

The transmittance of these acrylics were measured by a spectrophotometer (Shimazu Corporation MPS-2000). The transmittance of Acrylite#001

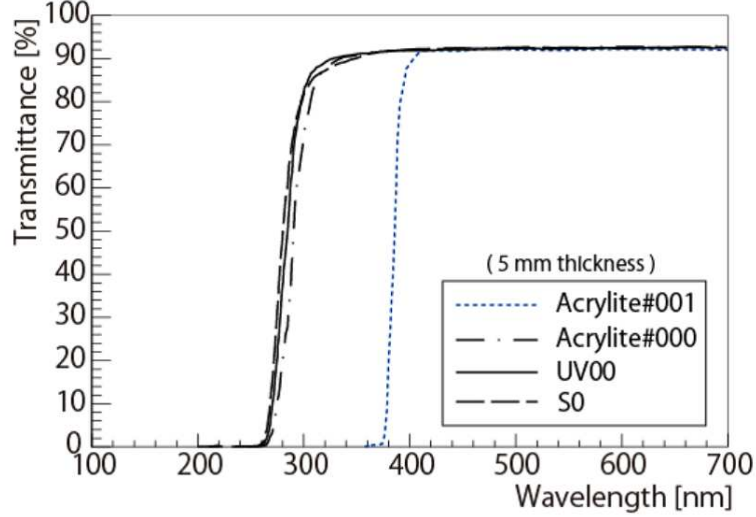


Figure 15: Transmittance of acrylics (Acrylite#001, Acrylite#000, UV00, S-0) with thicknesses of 5 mm measured by a spectrophotometer (Shimazu Corporation MPS-2000).

which was used for the previous prototype water Čerenkov detector (Sec. 3) falls down at around 380 nm. On the other hand, the transmittance of other acrylics fall down at around 280 nm.

Transmittance of Optical Coupling Grease A transmittance of an optical coupling grease, Saint-Gobain BC-630 ($n = 1.465$) which was taken from [15] is shown in Fig. 16. For a comparison, a nominal transmittance of an optical crystal, OKEN^{*11} BaF₂ ($n = 1.48$ ^{*12}) is also shown. Dashed lines for BaF₂ represent extrapolations of the data.

^{*9}Kuraray company, <http://www.kuraray.co.jp/>

^{*10}Nitto Jushi Kogyo company, <http://www.clarex.co.jp/>

^{*11}Ohyo Koken Kogyo company, http://www.oken.co.jp/web_oken/indexen.htm

^{*12}This value is at the wavelength of 400 nm.

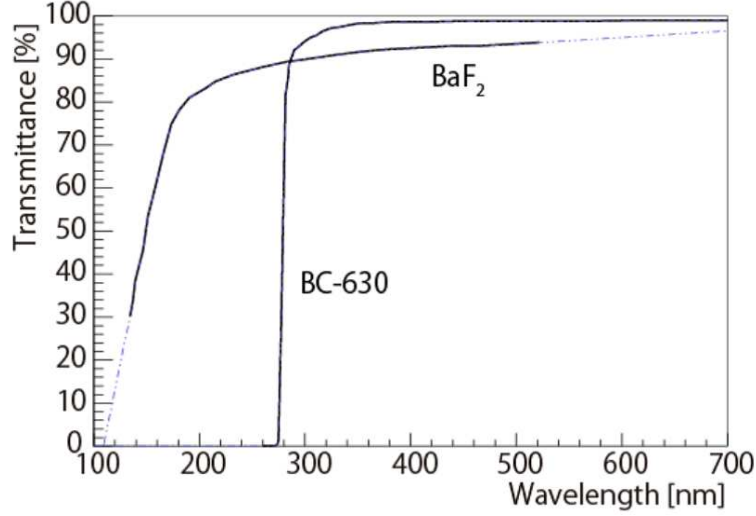


Figure 16: Transmittance of Saint-Gobain BC-630 [15] and OKEN BaF₂. Dashed lines for BaF₂ represent extrapolations of the data.

Transmittance of PMT Window Before a Čerenkov light reaches a PMT photocathode, the light has to pass through a PMT window. Nominal transmittance of PMT windows (UV transmitting glass (UVT), borosilicate glass (BSG)) are shown in Fig. 17 [16]. Dashed lines represent extrapolations of the data. The transmittance of UVT is higher in UV region compared to that of BSG.

PMT Quantum Efficiency Fig. 18 shows nominal quantum efficiencies of PMT photocathodes (bialkali (BA) and super bialkali (SBA)) [16]. The quantum efficiency of SBA is higher than that of BA by about 10% at the wavelength of 350 nm. Dashed lines represent extrapolations of the data.

Search for Better Configuration The number of Čerenkov photons as a function of the wavelength (Fig. 13) was multiplied by the transmittance of acrylic windows (Fig. 15), optical coupling greases (Fig. 16) and PMT windows (Fig. 17), and the PMT quantum efficiencies (Fig. 18) and the water absorption (Fig. 14) in order to search the best configuration using the above materials, and some of results at $y = 0$ cm using Experimental data 2 are shown in Fig. 19. The results were calculated for a π^+ with the momentum of

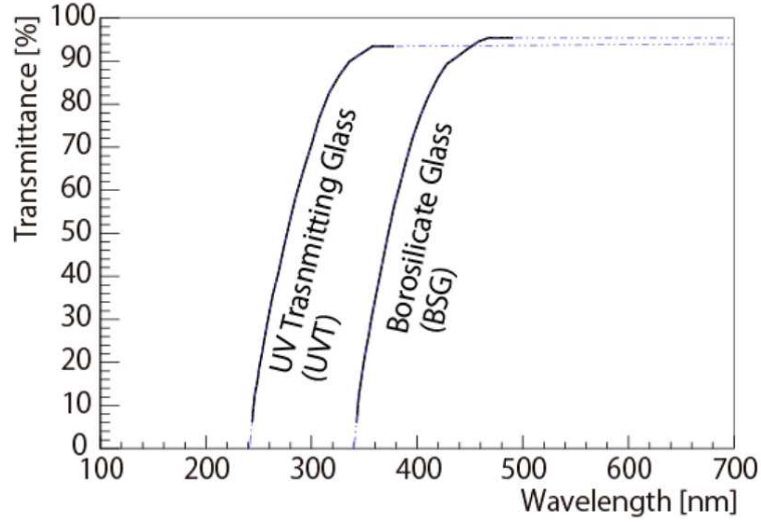


Figure 17: Nominal transmittance of PMT windows (UV transmitting glass (UVT), borosilicate glass (BSG)) [16]. Dashed lines represent extrapolations of the data.

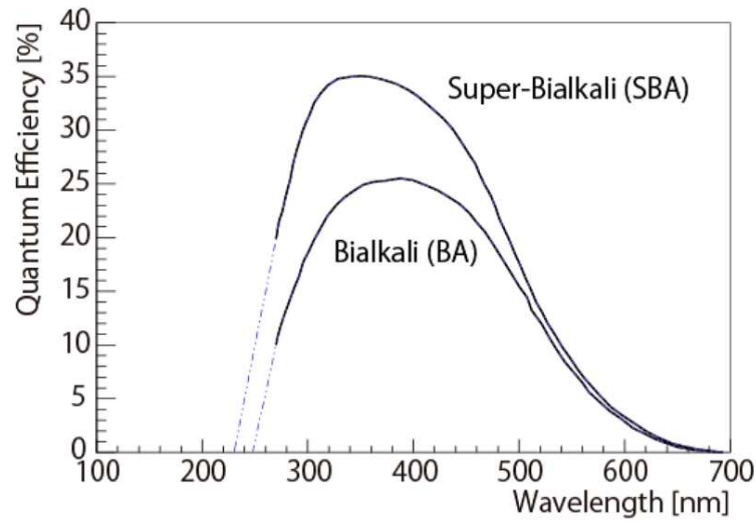


Figure 18: Quantum efficiencies of PMT photocathodes, bialkali(BA) and super bialkali (SBA) [16]. Dashed lines represent extrapolations of the data.

1.3 GeV/ c assuming that the path length of generated Čerenkov light in the container is $\frac{35.0}{\cos \theta_C}$ cm. The ordinate axis was normalized so as to make an in-

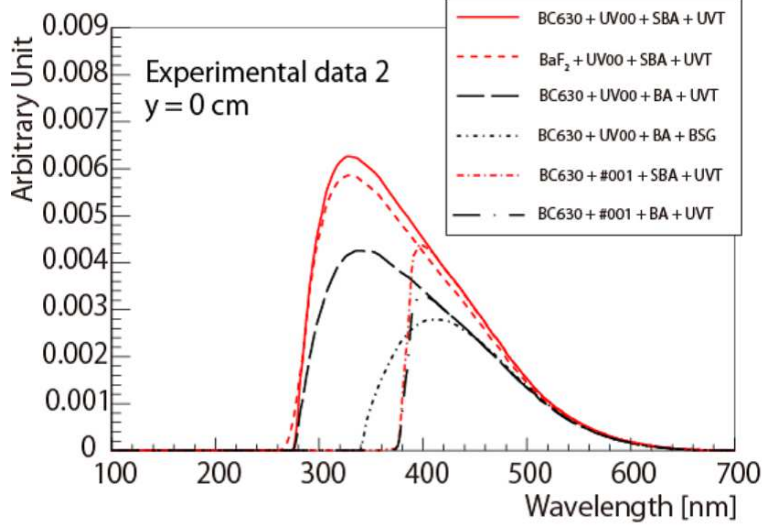


Figure 19: Expected Čerenkov light spectra with some of configurations at $y = 0$ using Experimental data 2. The ordinate axis was normalized so as to make an integral of the spectrum with a configuration of (BC-630+UV00+SBA+UVT) unity.

tegral of the spectrum with a configuration of (BC-630+UV00+SBA+UVT) unity. An integral of the spectrum is directly related to NPE. Results of integration for some of typical configurations are shown in Table. 3. It is noted that the integral with the configuration of ① (BC-630+UV00+SBA+UVT) using Experimental data 2 is normalized to be unity as well as Fig. 19. The prototype water Čerenkov detector which was used for the positron beam test (Sec. 3) adopted a configuration of ⑦ (BC-630+#001+SBA+UVT) in Table. 3. If one changes the acrylic window (Acrylite#001) to UV transmitting one such as UV00 (configuration of ①), the NPE is expected to significantly improve compared to that of the previous configuration. This significant improvement is caused by a recovery of the light spectrum for UV region as shown in Fig. 19. Thus a cosmic-ray test to determine a window material maximizing NPE was done, and described in the next section.

Table 3: Integration of Fig 19 for some of typical configurations.

Configuration	Data of Water Absorption	Relative NPE
① BC-630+UV00+SBA+UVT	1	0.916
	2	1
② BaF ₂ +UV00+SBA+UVT	1	0.866
	2	0.948
③ BaF ₂ +S-0+SBA+UVT	1	0.868
	2	0.952
④ BaF ₂ + $\#000$ +SBA+UVT	1	0.848
	2	0.923
⑤ BC-630+UV00+BA+UVT	1	0.675
	2	0.73
⑥ BC-630+UV00+BA+BSG	1	0.396
	2	0.404
⑦ BC-630+ $\#000$ +SBA+UVT	1	0.438
	2	0.444
⑧ BC-630+ $\#000$ +BA+UVT	1	0.352
	2	0.356

4.3 Cosmic-ray Test for the Window Material Optimization

4.3.1 Experimental Setup

Fig. 20 shows a schematic drawing of experimental setup for the window material optimization using cosmic-rays. The container was the same as that in used the beam test (Sec. 3), but a cap part was newly designed and constructed in order to easily change the acrylic windows. A magnified drawing of the cap part is shown in Fig. 21. A PMT of H11284-100UV was attached on the UVT acrylic window using BaF_2 . The cap part was attached to the container using a PP band, and the container was filled by pure water. An LED light was attached on the PMT near by the photocathode for the use of the NPE calibration as shown in Sec. 3.3.1. The container was sandwiched between two plastic scintillation detectors which were used as data taking triggers. The plastic scintillation detectors were set at $y = 0$ cm during this test. In the test, NPEs with UVT acrylic materials of UV00, S-0 and

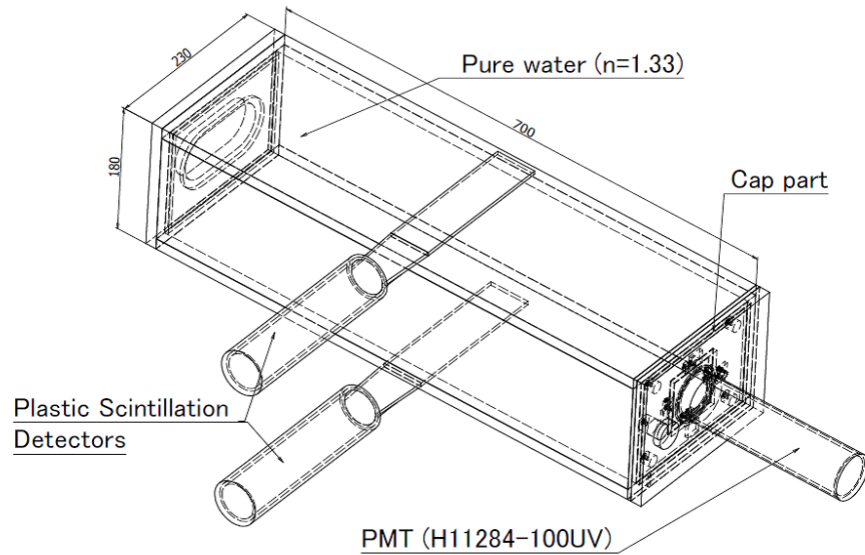


Figure 20: A schematic drawing of the experimental setup of a cosmic ray test to optimize an acrylic window material. The unit is mm.

Acrylite#000 (Fig. 15) were studied, and compared with Acrylite#001.

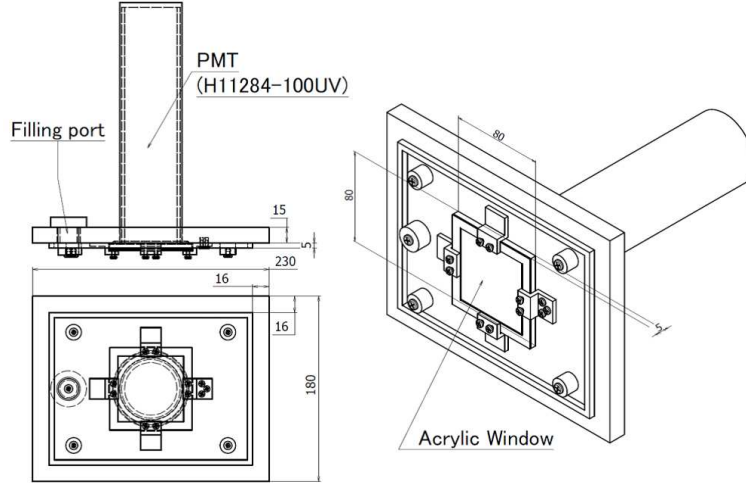


Figure 21: A magnified drawing of the cap part which was designed and constructed to easily change the acrylic windows during the test. The unit is mm.

4.3.2 Analysis and Results

A conversion from ADC to NPE was done by using data with LED light as shown in Sec. 3.3.1. Fig. 22 shows a typical NPE histogram. The NPE spectrum was fitted with a single-Gaussian function to obtain the mean value, and used as a result.

The NPE results for UV00, S-0 and Acrylite#000 were summarized in Table. 4. Errors on the results are statistical and systematic ($= \sigma_{calb.}$, Sec. 5.2.2). Each acrylic window was tested twice to check the reproducibility, and the NPEs of two measurements for each window usage were consistent within the errors. All of tested windows were able to achieve larger NPEs than that of Acrylite#001 by $\geq 50\%$. The NPEs with UV00 and S-0 were larger than that of Acrylite#000 by $\geq 5\%$ though a difference of NPEs between UV00 and S-0 was not observed within the errors. As a result, we have determined to use UV00 as the window material.

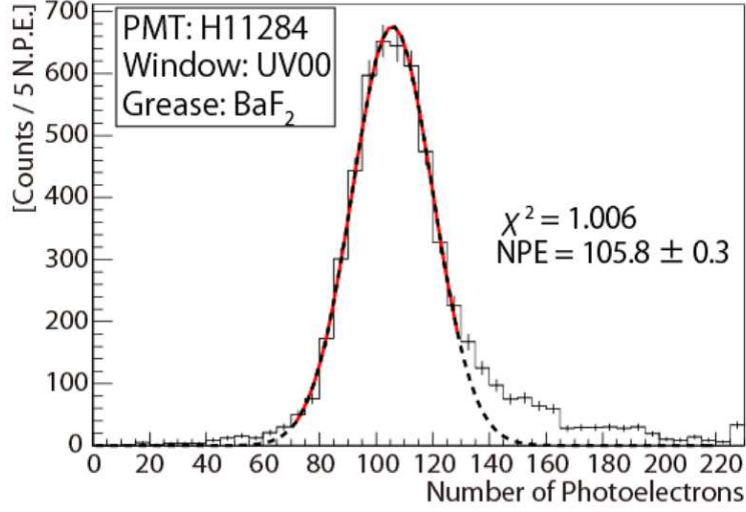


Figure 22: A typical NPE histogram obtained in a test to optimize the acrylic window material. The NPE histogram was fitted by a single-Gaussian function, and the mean value was used as a result.

Table 4: NPE results using acrylic window materials of UV00, S-0 and Acrylite#000. Each window was tested twice to check a reproducibility of the NPE measurement. Errors on the results are statistical and systematic ($= \sigma_{calb.}$, Sec. 5.2.2).

Window material	NPE	Trial
UV00	$105.8 \pm 0.3 \pm 1.1$	1
	$103.9 \pm 0.6 \pm 1.0$	2
S-0	$106.6 \pm 0.3 \pm 1.1$	1
	$105.4 \pm 0.6 \pm 1.1$	2
Acrylite#000	$96.4 \pm 0.4 \pm 1.0$	1
	$99.6 \pm 0.5 \pm 1.0$	2

5 New Prototype Water Čerenkov Detector

A window material was optimized as shown in the previous section. A new prototype was constructed with the new window material which has the higher transmittance in UV region. In this section, design of the new prototype and the performance test with cosmic-rays are described.

5.1 Design

The design of the new prototype of water Čerenkov detector is similar to that of the previous prototype as shown in Sec. 3.1 except for the window material and cap part. Fig. 23, Fig. 24, Fig. 25 and Fig. 26 show drawings of the new prototype water Čerenkov detector. UV00 was chosen (Sec. 4.3.2)

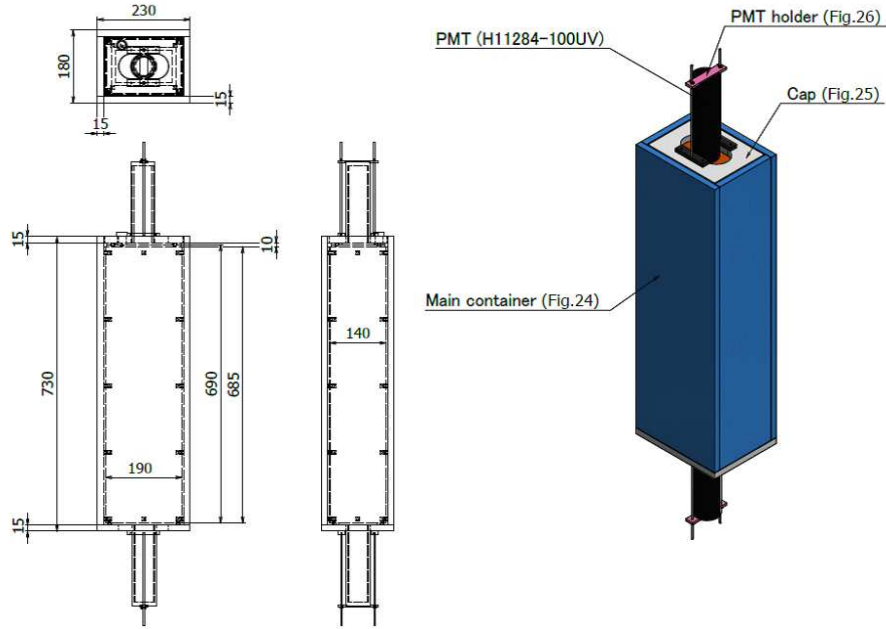


Figure 23: A drawing of the new prototype water Čerenkov detector which was constructed with the optimized window material (UV00). The unit is mm.

and used as the window material which was bond on an inner surface of container box by polymerization. The cap part was designed as shown in

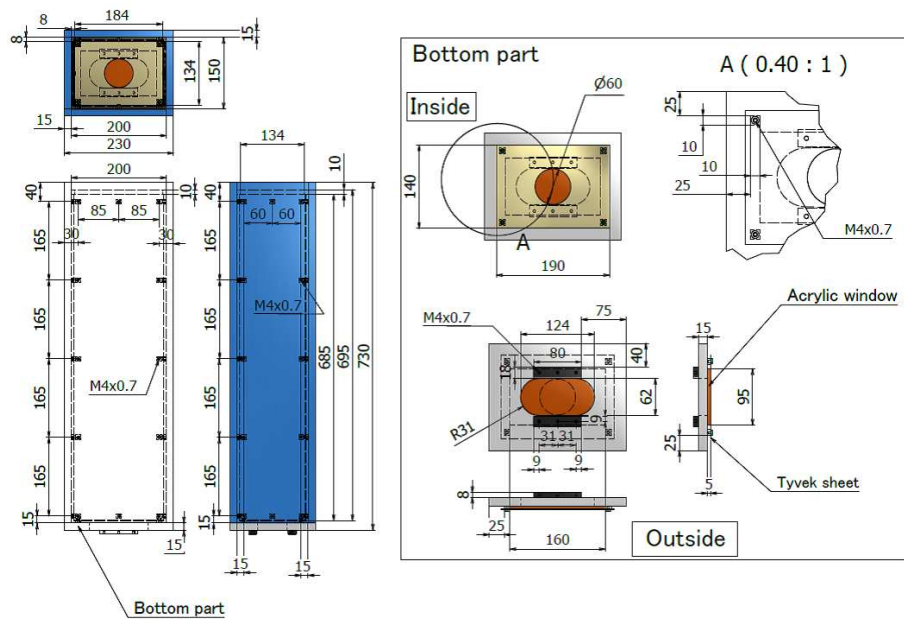


Figure 24: A drawing of the container box of new prototype water Čerenkov detector. The unit is mm.

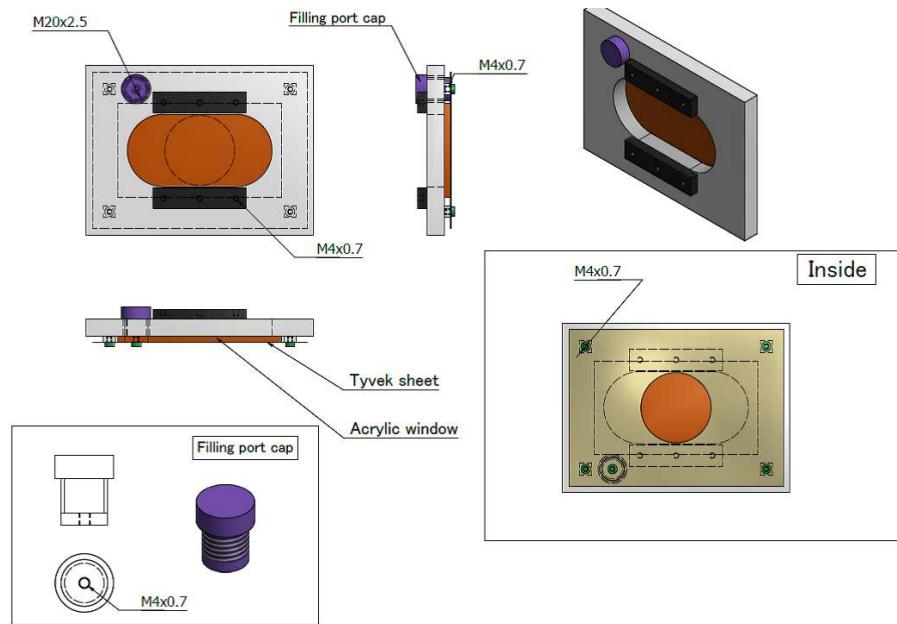


Figure 25: A drawing of the cap part of the new prototype water Čerenkov detector. The unit is mm.

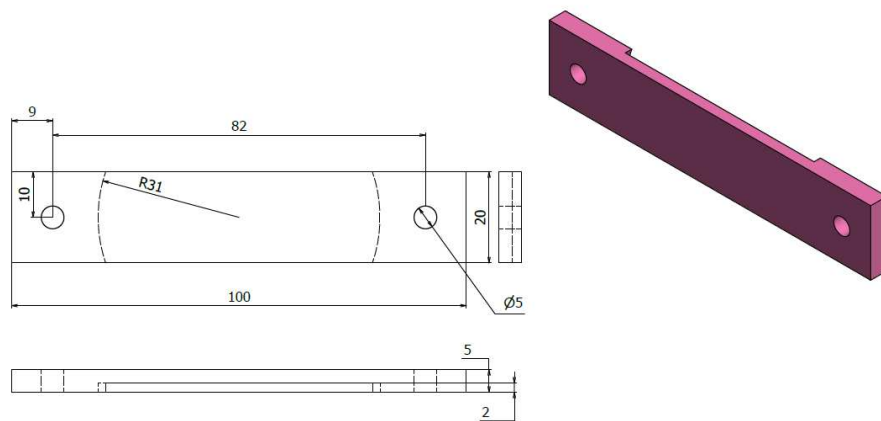


Figure 26: A drawing of the PMT holder of new prototype water Čerenkov detector. The unit is mm.

Fig. 27. The size of cap part is smaller compared to the opening mouth of container box. There is a frame on the inner surface of container, and the cap was put on the frame. Then, a caulking material (CEMEDINE, Bathcaulk N^{*13}) was filled into a gap between the cap part and container box to seal the detector.

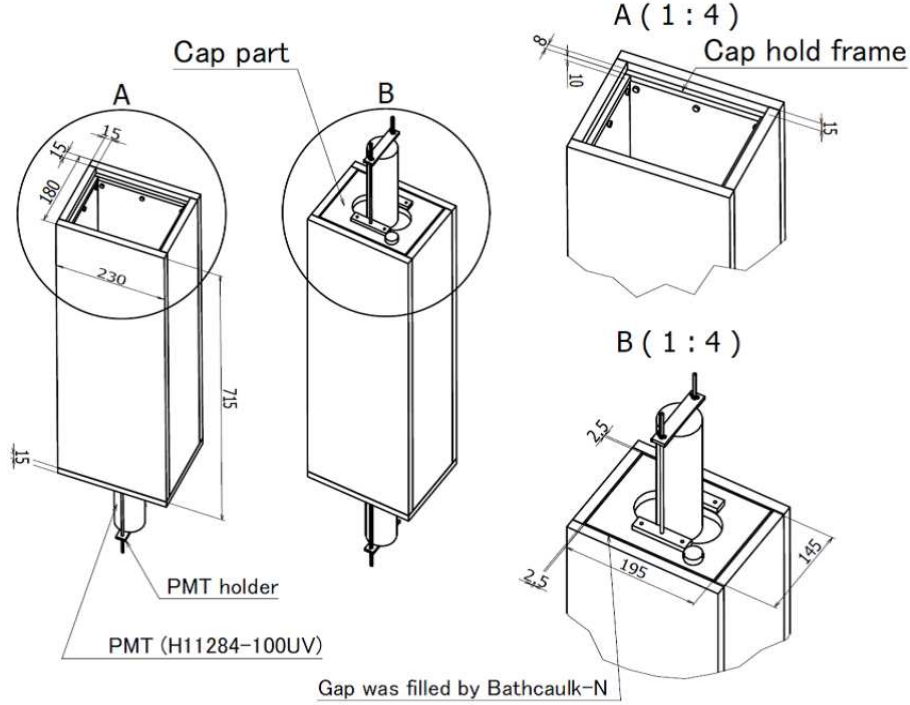


Figure 27: A design of cap part of new prototype water Čerenkov detector.

5.2 Cosmic-ray Test

In the cosmic-ray test, NPE dependencies on the incident particle position, applied HV and time after the construction were measured. Furthermore, systematic error on NPE due to calibration, PMT individual performance difference and effect of optical coupling grease were investigated.

^{*13}CEMEDINE Co., <http://www.cemedine.co.jp/e/index.html>

5.2.1 Experimental setup

An experimental setup was similar to that in the cosmic-ray test shown in Sec. 4.3.1. The prototype water Čerenkov detector was sandwiched by two plastic scintillation detectors which were used as trigger counters for data taking. The two trigger counters were able to be moved to see an NPE dependence on the incident particle position. Fig. 28 shows a photograph of the experimental setup. An LED light which was used for the NPE calibration

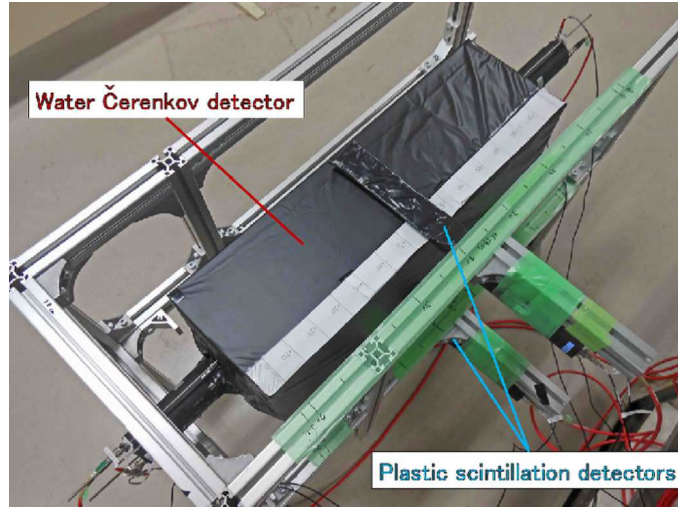


Figure 28: A photograph of the experimental setup of cosmic-ray test for the prototype water Čerenkov detector.

was attached just beside a PMT photocathode^{*14}.

5.2.2 LED Calibration and Systematic Error

The ADC channels per a single photoelectron is obtained by fitting an ADC histogram with LED as shown in Fig. 6. The calibration result might be fluctuated by electric circuit conditions due to temperature, histogram fitting conditions and the other hidden factors. Calibration data with the same experimental setting were taken in a period of one week. The obtained ADC channels per a single photoelectron for H11284-100UV PMTs with serial

^{*14}Outside of the container box.

numbers of ZK6920 (-2000 V) and ZK6922 (-2000 V) were plotted in Fig. 29. It is found that the standard deviations were $< 1\%$ for both PMTs. In the

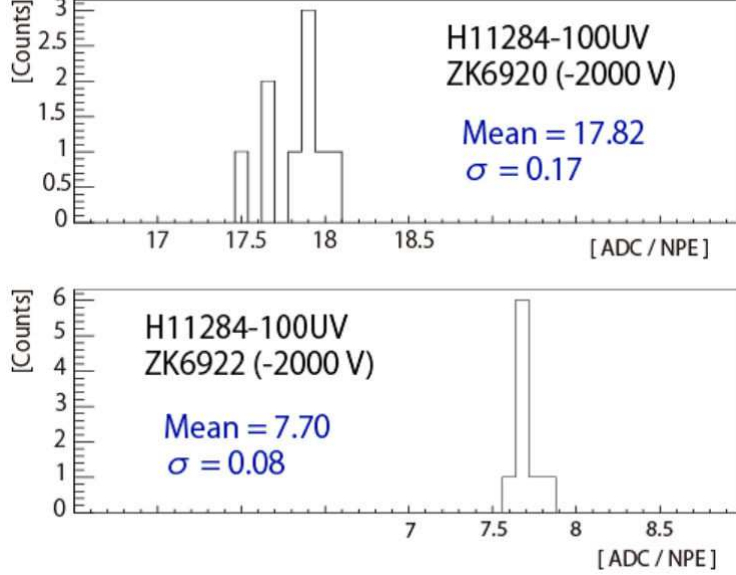


Figure 29: Nine of obtained LED calibration data for H11284-100UV PMTs with serial numbers of ZK6922 (-2000 V) and ZK6920 (-2000 V) in a period of one week.

present report, 1% ($\equiv \sigma_{calb.}$) is used as a systematic error of resulting NPE.

5.2.3 NPE Detection Performance

The NPEs detected by TOP (ZK6922, -2000 V) and BOTTOM (Z6920, -2000 V) PMTs at $y = 0$ cm^{*15} were:

$$\text{NPE}_{(\text{TOP}, \text{ZK6922})}^{\text{Cosmic}} = 109.6 \pm 0.5^{\text{stat.}} \pm 1.1^{\text{sys.}}, \quad (11)$$

$$\text{NPE}_{(\text{BOT}, \text{ZK6920})}^{\text{Cosmic}} = 97.9 \pm 0.5^{\text{stat.}} \pm 1.1^{\text{sys.}}. \quad (12)$$

A summed NPE obtained by fitting to a summed NPE histogram was:

$$\text{NPE}_{(\text{sum})}^{\text{Cosmic}} = 207.7 \pm 0.9^{\text{stat.}} \pm 2.9^{\text{sys.}}. \quad (13)$$

^{*15}Coordinates are defined as Fig. 4.

A difference between TOP and BOTTOM NPEs would mainly originate from how the Tyvek sheet was attached inside container as discussed quantitatively in Sec. 5.2.6.

5.2.4 y -position Dependence

The NPE dependence on an incident particle position is rather stronger in y -coordinate than that in x -coordinate as shown in the positron beam test (Fig. 11). Thus, the y -position dependence was investigated by changing position of trigger scintillation detectors in y -direction. Fig. 30 shows resulting NPEs as a function of y -position. The NPEs were normalized to be unity at $y = 0$ cm. The y -position dependence is asymmetric even for the summed

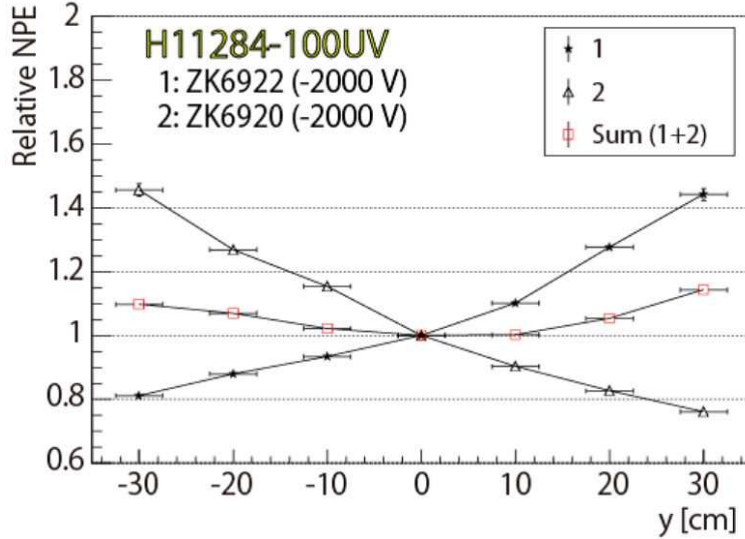


Figure 30: A y -position dependence of TOP (labeled as 1), BOTTOM (labeled as 2) and sum of TOP and BOTTOM.

NPE. The asymmetric dependence would be caused by asymmetric tendencies of photon yield (Fig. 13) and absorption coefficients of water (Fig. 14) for a Čerenkov light with the different wavelength. For a Čerenkov light with the shorter wavelength, the light yield is larger, but the absorption coefficient of water is larger as well. The NPE variation depending on the incident y -position was obtained to be $< +20\%$.

5.2.5 HV Dependence

Supplied High Voltages (HVs) for PMTs were varied from -1800 V to -2100 V, and the HV dependence of NPE was investigated. Fig. 31 shows the HV dependence of summed NPE (sum of TOP and BOTTOM PMTs). Statistical errors were smaller than a size of marker, and the systematic errors were represented by brackets ($= \sigma_{calb.}$, Sec. 5.2.2). It was found that there is no HV dependence within the errors.

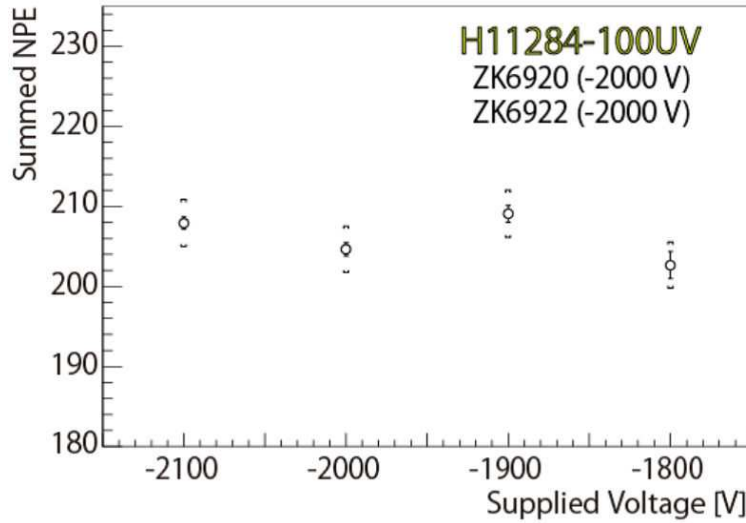


Figure 31: A HV dependence of summed NPE (sum of TOP and BOTTOM PMTs). There is no dependence on HV within the errors.

5.2.6 PMT Individual Performance Difference

An NPE depends on an individual performance of PMT, and it was studied by measuring NPEs with PMTs of different serial numbers. Table. 5 shows serial numbers, applied HVs, ADC channels per a single photoelectron (ADC/NPE) and obtained NPEs at $y = 0$ cm.

There are systematic differences between NPEs which are detected by TOP and BOTTOM PMTs due to mainly how the Tyvek sheets were attached inside container. In order to obtain a geometrical factor ($\equiv G_{T2B}$) that normalizes TOP NPE to that of BOTTOM, data swapping TOP and

Table 5: NPE results using H11284-100UV PMTs with different serial numbers at $y = 0$ cm. Normalized NPEs which are shown in the last column were obtained by using the geometrical factor, G_{T2B} that normalizes a TOP NPE to BOTTOM one. In this table, BOTTOM NPEs were divided by G_{T2B} to be compared from each other.

Serial number	HV [V]	ADC/NPE	PMT position	NPE	Normalized NPE
ZK6919	-2250	11.18	BOTTOM	104.8 ± 0.4	121.9 ± 0.4
ZK6920	-2000	19.08	BOTTOM	97.9 ± 0.5	114.4 ± 0.6
ZK6922	-2000	7.21	TOP	109.6 ± 0.5	109.6 ± 0.5
ZK6925	-2250	7.04	TOP	113.0 ± 0.4	113.0 ± 0.4
ZK7295	-2000	6.31	BOTTOM	101.4 ± 1.0	117.9 ± 1.2
ZK7296	-2000	4.19	BOTTOM	102.1 ± 0.5	118.7 ± 0.5
ZK7298	-2000	9.97	BOTTOM	97.7 ± 0.7	113.6 ± 0.8
ZK7299	-2000	6.12	TOP	112.2 ± 0.6	112.2 ± 0.6
ZK7300	-2250	7.63	TOP	110.7 ± 0.6	110.7 ± 0.6
ZK7301	-2250	6.31	TOP	126.7 ± 0.4	126.7 ± 0.4
ZK7302	-2250	7.87	BOTTOM	102.5 ± 0.4	119.2 ± 0.4
ZK7303	-2250	4.20	BOTTOM	113.5 ± 0.4	131.9 ± 0.5
ZK7304	-2250	5.21	TOP	103.4 ± 0.6	103.4 ± 0.6
ZK7305	-2250	4.44	BOTTOM	109.4 ± 0.7	127.2 ± 0.8
ZK7306	-2250	3.80	TOP	117.1 ± 0.5	117.1 ± 0.5
ZK7307	-2250	13.50	TOP	124.7 ± 1.0	124.7 ± 1.0
ZK7308	-2250	11.82	TOP	115.8 ± 0.3	115.8 ± 0.3
ZK7309	-2250	7.71	BOTTOM	100.3 ± 0.7	116.7 ± 0.8
ZK7310	-2250	4.58	BOTTOM	98.7 ± 0.6	114.7 ± 0.7
ZK7311	-2000	10.88	BOTTOM	94.4 ± 0.5	109.8 ± 0.5
ZK7312	-2250	6.46	TOP	114.0 ± 0.5	114.0 ± 0.5
ZK7313	-2000	7.81	TOP	111.1 ± 0.4	111.1 ± 0.4
ZK7315	-2250	8.84	TOP	112.2 ± 0.4	112.2 ± 0.4
ZK7316	-2250	3.31	TOP	116.3 ± 0.5	116.3 ± 0.5

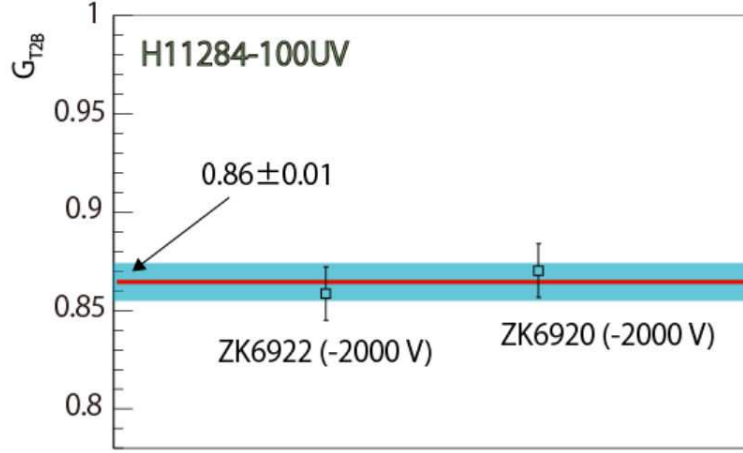


Figure 32: BOTTOM NPE ratios relative to TOP one for the PMTs of ZK6922 and ZK6920. A fitting result is represented by a line, and the geometrical factor was obtained to be $G_{T2B} = 0.86 (\pm 0.01)$.

BOTTOM PMTs were taken. Table. 6 shows results of the swapping test. BOTTOM NPE ratios relative to TOP ones are shown in Fig 32. The ge-

Table 6: NPE results with PMTs of ZK6922 (H11284-100UV) and ZK6920 (H11284-100UV) when they were attached on the TOP and BOTTOM sides. The errors are statistical.

	ZK6922 (-2000 V)	ZK6920 (-2000 V)
TOP	109.6 ± 0.5	112.5 ± 0.5
BOTTOM	94.1 ± 0.5	97.9 ± 0.3

ometrical factor was obtained to be $G_{T2B} = 0.86 (\pm 0.01)$ by fitting to the results as represented by a line in Fig. 32.

Normalized NPEs using G_{T2B} to be compared from each other are shown in the last column of Table. 5. The BOTTOM NPEs were normalized to those of TOP in the table (BOTTOM NPEs were divided by G_{T2B}). The center values of normalized NPEs were filled in a histogram, and shown in the top figure in Fig. 33. A mean value and a standard deviation were obtained to be 116 and 7 (= 6%), respectively. The 6% standard deviation

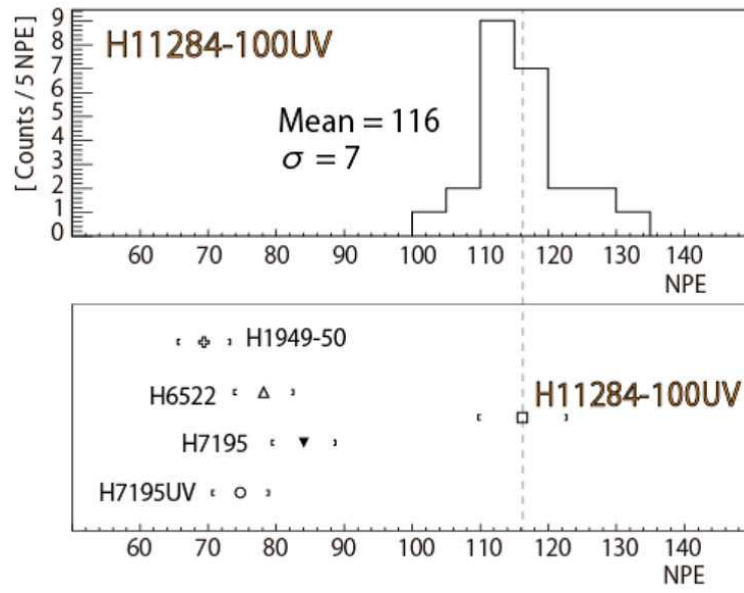


Figure 33: (Top) A histogram filled with center values of normalized NPEs by H11284-100UV PMTs (see also Table. 5). (Bottom) A comparison of NPEs among different types of PMTs.

also includes errors due to the calibration ($\sigma_{calib.} = 1\%$), reproducibility of PMT attachment and statistic ($\leq 1\%$). The errors of reproducibility is expected to be smaller or comparable level to that of the calibration ($\sigma_{calib.}$) as shown in Table. 4 and Table. 8. Thus, the PMT individual performance difference was estimated to be $\sqrt{6^2 - 1^2 - 1^2 - 1^2} \simeq 6\%$ ($\equiv \sigma_{PMT}$).

5.2.7 PMT Difference

To confirm the PMT choice of H11284-100UV that has a super bialkali photocathode and UV transmitting window (SBA+UVT), other types of Hamamatsu PMTs (H6522, H1949-50, H7195, H7195UV) were tested with cosmic-rays. The NPE results were shown in Table. 7 and bottom figure of Fig. 33. Errors on the results are statistical and σ_{PMT}^{*16} . It was found that a PMT of H11284-100UV is able to detect larger NPE than the other types of PMTs by more than 30%.

Table 7: NPE measurement results of H11284-100UV (Sec. 5.2.6), H6522 (BA+UVT), H1949-50 (BA+BSG), H7195 (BA+BSG) and H7195UV (BA+UVT). Errors on the results are statistical and σ_{PMT} .

PMT			NPE
Type	Photocathode + Window	Serial Number	
H11284-100UV	SBA + UVT	-	116 ± 7 (Sec. 5.2.6)
H6522	BA + UVT	LA1537	$78.2 \pm 0.3 \pm 4$
H1949-50	BA + BSG	WA6589	$69.4 \pm 0.3 \pm 4$
H7195	BA + BSG	RD7198	$84.1 \pm 0.3 \pm 5$
H7195UV	BA + UVT	LA1528	$74.8 \pm 0.3 \pm 4$

5.2.8 An Effect of Optical Coupling Grease

To see an NPE difference between with and without the optical coupling grease, data without the use of the grease were taken and compared. The test was proceeded as follows:

^{*16}The systematic error ($\sigma_{calib.}$) is negligible small compared to σ_{PMT}

- The optical coupling grease (Saint-Gobain BC-630) was used between the acrylic windows and PMTs for both TOP and BOTTOM PMTs in the first trial (Trial 1).
- Then, the grease for BOTTOM PMT was removed, and the PMT and acrylic window were only physically attached (Trial 2).
- Finally, the grease was used for BOTTOM PMT again to check a reproducibility (Trial 3).

Table. 8 shows the NPE results. The errors on the results are statistical and systematic ($\sigma_{calib.}$). It was found that the NPE is reduced by about 35%

Table 8: NPE results of a test to study the effect of the optical coupling grease (Saint-Gobain BC-630).

Trial	ZK6922 (-2000 V) [TOP]	ZK6920 (-2000 V) [BOTTOM]
1	$109.6 \pm 0.5 \pm 1.1$	$97.9 \pm 0.3 \pm 1.0$
2	$114.3 \pm 0.7 \pm 1.1$	$63.6 \pm 0.3 \pm 0.6$ (No Grease)
3	$111.6 \pm 0.5 \pm 1.1$	$98.2 \pm 0.4 \pm 1.0$

when the optical coupling grease is not used. This reduction would be caused by the air gap between the PMT and acrylic window. If there is an air gap between a PMT window and acrylic window, the total reflection occurs for a photon with a certain incident angle at the boundary.

5.2.9 Long term stability

The water Čerenkov detector should work stably during a term of experiment which would be around a month. In order to check a long term stability, the NPE measurement with cosmic-ray was done for 100 days. Fig. 34 shows a result of the measurement. The NPEs was normalized so as to make a mean value of obtained NPEs unity. The prototype water Čerenkov detector worked stably for 100 days.

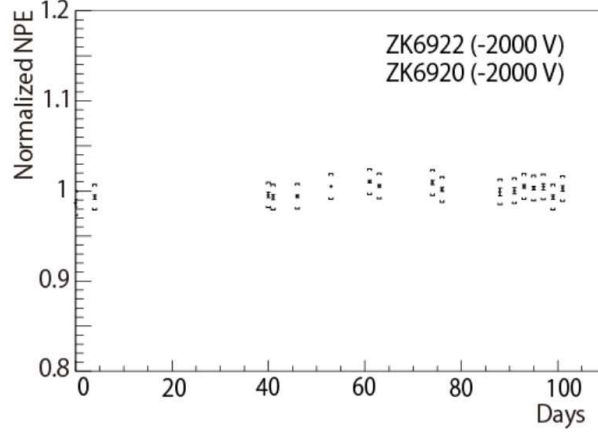


Figure 34: A time dependence of NPE in the cosmic-ray test. The prototype water Čerenkov detector was able to work stably for 100 days.

6 Expected Proton Rejection Power by a Monte Carlo Simulation

The performance of one segment of water Čerenkov detector was discussed in the above sections. In the experiment, J-PARC E05, however, twelve segments of water Čerenkov detectors will be installed in two layers as shown in Fig. 35. A Monte Carlo simulation (Geant4 [6]) was done in order to study the performance of water Čerenkov detector as a total system of twelve segments in S-2S. Expected performances of a proton rejection efficiency and a K^+ survival ratio using the Monte Carlo simulation are described in this section.

6.1 Setup and Conditions in the Monte Carlo Simulation

In the simulation, S-2S is modeled as Fig. 1. A magnetic field of S-2S was calculated by a software for magnetic field calculation using three dimensional finite element method, Opera3D (TOSCA) [17]. Materials were defined for S-2S magnets (QQD), TOF detector and water Čerenkov detector in the sim-

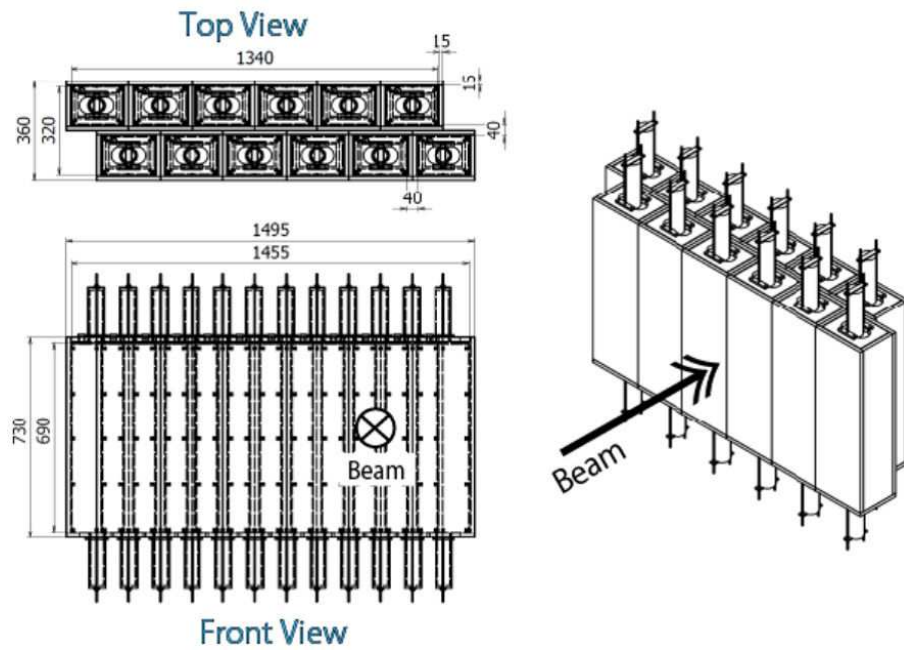


Figure 35: A drawing of twelve segments of the water Čerenkov detectors. One layer consists of six segments. Two layers are set covering their inefficient regions from each other.

ulation^{*17}. The water Čerenkov detector was placed at 2.41 m downstream of the dipole magnet exit in a beam direction. Particles were generated at a point of 600 mm upstream of a Q1 magnet entrance, where a target is planned to be installed. A mean NPE in the water Čerenkov detector when a $\beta = 1$ particle is perpendicularly incident at the center is assumed to be 200 (sum of TOP and BOTTOM NPEs) although the NPE was obtained to be $207.7 \pm 0.9 \pm 2.9$ in the cosmic-ray test as shown in Sec. 5.2.3. The mean NPE value was randomly varied by $\pm 6\%$ event by event to take into account the PMT individual performance difference ($\sigma_{\text{PMT}} = 6\%$) shown in Sec. 5.2.6. The NPE position dependence which was represented in Sec. 5.2.4 was taken into account by scaling NPE depending on an incident position of a particle. A path length of an incident particle in a medium of the water Čerenkov detector depends on the incident position and angle. Thus, the path length scaling was applied for the NPE calculation event by event (Eq. (1)). Fig. 36 shows displayed particle tracks in the simulation. Particles are converged respectively in longitudinal and transverse directions by two quadrupole magnets (Q1 and Q2), and bent in a dispersive plane by a dipole magnet (D) transporting the particles to the particle detectors.

Table 9: Conditions in the S-2S Monte Carlo simulation.

Particle Generation at the target point	Distribution	Spherical uniform
	Momentum [GeV/c]	1.10 - 1.75
	Angle [deg]	0 - 25
Process	Electromagnetic: ON Hadronic: ON	
Detector Materials	TOF (2 ^t cm plastic scintillator) WC (pure water + acrylic)	
Assumed NPE in WC	200 ($\beta = 1$ particle)	

Fig. 36 shows particle distributions (momentum vs. x , x' vs. x , y vs. x , y' vs. y) at a reference plane which was set at 3 cm upstream of a front surface of water Čerenkov detector. In order to cover the momentum region from 1.2 to 1.6 GeV/c, the geometry of water Čerenkov detector is designed as Fig. 35.

^{*17}Others were set as vacuum.

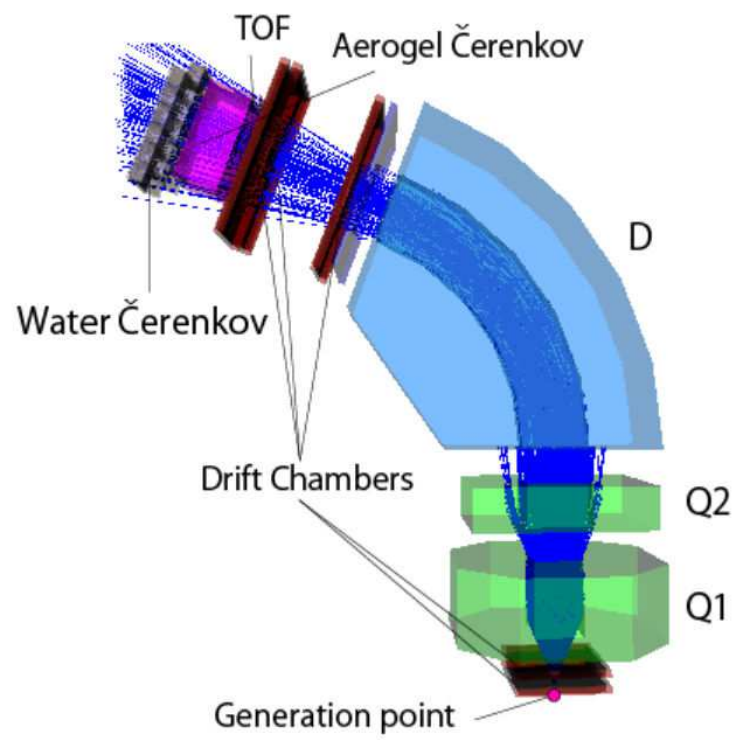


Figure 36: Displayed tracks in the S-2S Monte Carlo simulation.

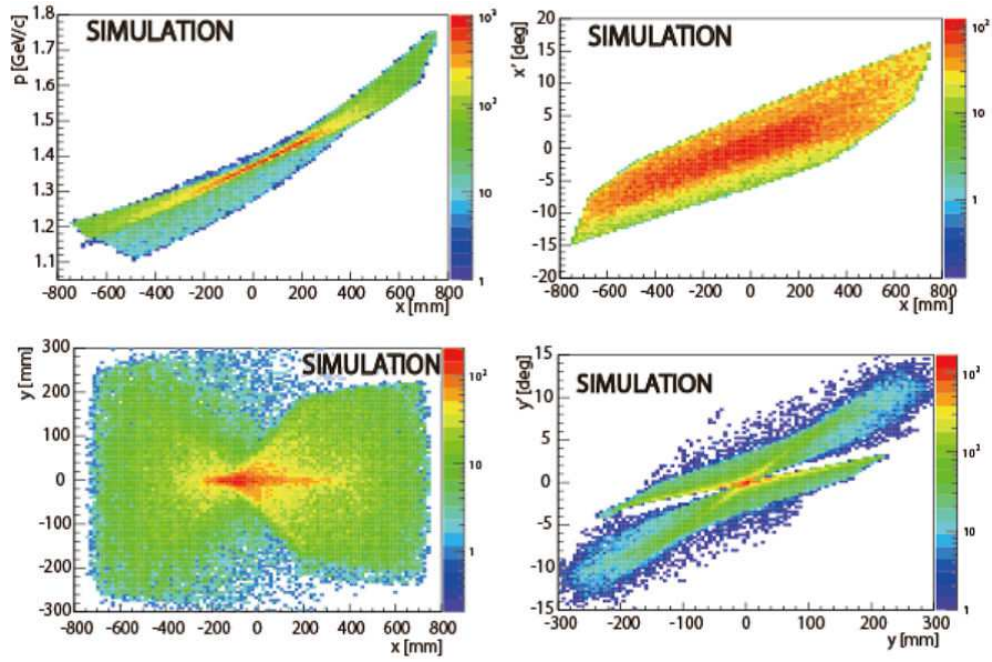


Figure 37: Particle distributions at the reference plane which was set at 3 cm upstream of the water Čerenkov detector front surface in the S-2S Monte Carlo simulation.

6.2 Analysis and Results

Fig. 38 shows the NPE distributions in the first (WC1) and second (WC2) layers of water Čerenkov detectors for protons, K^+ s and π^+ s with the same number of events for each kind of particle. The NPE distributions in WC2 are broader than those in WC1 due to secondary particles that originate from some reaction and decay processes. Two dimensional plots of NPE vs.

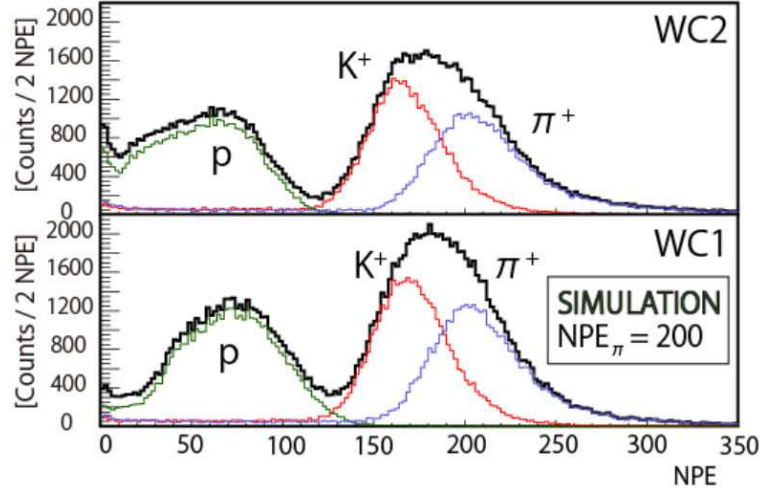


Figure 38: NPE distributions for protons, K^+ and π^+ s in the first and second layers (WC1, WC2) of water Čerenkov detector.

x position at the reference plane^{*18} for WC1 and WC2 are shown in Fig. 39. Inefficient region in a layer is designed to be covered from each other.

In the experiment, protons will be suppressed on-line by using a logical condition as follows:

$$WC1 \oplus WC2. \quad (14)$$

The $WC1$ and $WC2$ represent that an incident particle serves NPE which is above a certain threshold in each layer of the water Čerenkov detector. In order to estimate on-line proton rejection efficiency, an event select condition was applied as the following:

$$WC1^{sim} \oplus WC2^{sim} \quad (15)$$

^{*18}At 3 cm upstream of the front surface of water Čerenkov detector.

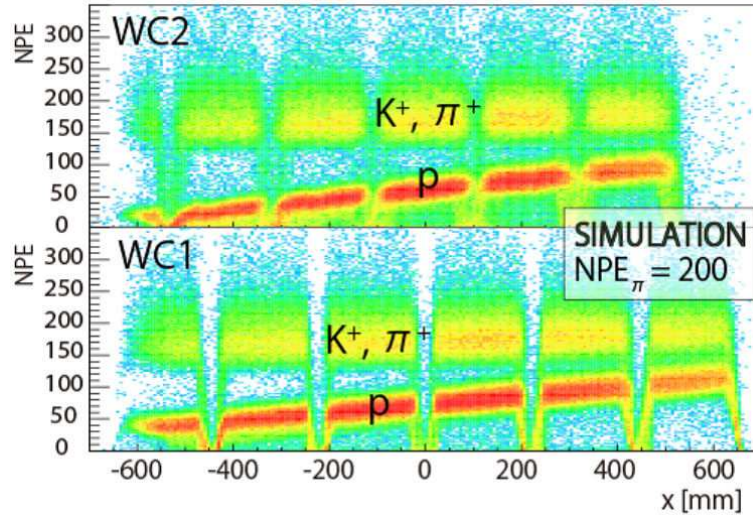


Figure 39: Distributions of NPE vs. x -position at the reference plane for WC1 and WC2 in the Monte Carlo simulation. Inefficient region in a layer is designed to be covered from each other. Assumed NPE in the water Čerenkov detector for a $\beta = 1$ particle is 200.

where,

$$WC1^{sim} = \sum_{i=1}^6 \left(NPE_{(WC1)}^i > x_1^i \right), \quad (16)$$

$$WC2^{sim} = \sum_{i=1}^6 \left(NPE_{(WC2)}^i > x_2^i \right). \quad (17)$$

The superscript i represents a segment number in each layer. The selection thresholds, $x_{1,2}^i$ were determined so that $> 95\%$ K^+ s survive in each segment.

Survival ratios for a proton and K^+ ($SR_{(p,K^+)}$) are defined as the following:

$$SR_{(p,K^+)} = \frac{N_{(p,K^+)}}{N_{(p,K^+)}^{Ref}} \quad (18)$$

where $N_{(p,K^+)}$ is the number of events with the event selection of Eq. (15), and $N_{(p,K^+)}^{Ref}$ is that without the event selection at the reference plane. Fig. 40 shows $SR_{(p,K^+)}$ as a function of particle momenta at the particle generation point. It shows that the water Čerenkov detector is expected to achieve

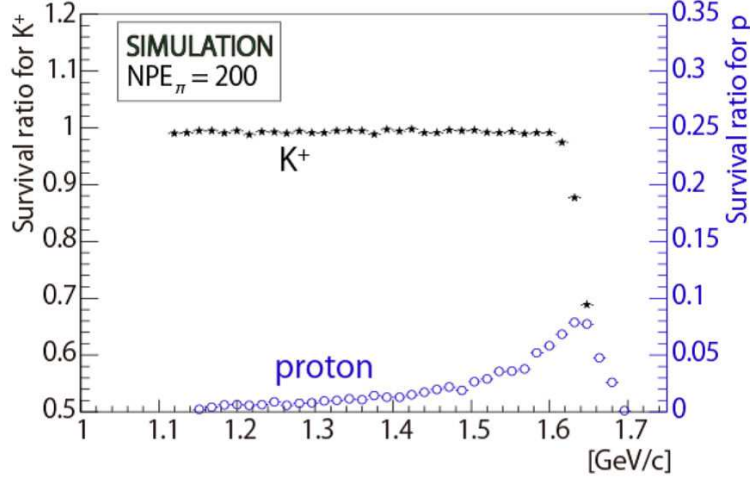


Figure 40: The survival ratios for protons and K^+ s ($SR_{(p,K^+)}$) as a function of particle momenta at the particle generation point.

$> 90\%$ protons rejection efficiency keeping $> 95\%$ survival ratio for K^+ s in the whole S-2S momentum acceptance. The shown performance fulfills our requirements for the Ξ^- hypernuclear spectroscopy at J-PARC.

7 Summary

A Ξ^- hypernuclear spectroscopy is planned at J-PARC K1.8 beam line by using the (K^-, K^+) reaction to investigate the ΞN interaction (J-PARC E05 experiment). A new magnetic spectrometer, S-2S which possesses high momentum resolution ($\Delta p/p \simeq 5.0 \times 10^{-4}$ in FWHM) for a momentum region from 1.2 to 1.6 GeV/ c is being constructed for a scattered K^+ detection. Protons and π^+ s are expected to be detected in S-2S as major background sources. Counting rates for protons and π^+ s are estimated to be around a thousand times higher than that of K^+ s according to a Monte Carlo simulation with a safety multiplication factor of five on the background particles. In order to suppress these background particles on-line, aerogel ($n = 1.05$) and water ($n = 1.33$) Čerenkov detectors are necessary and designed to be installed in S-2S.

We have constructed prototypes of the water Čerenkov detector and tested by irradiating positron beams and cosmic-rays. The latest prototype was able to achieve NPE > 200 for $\beta = 1$ charged particles with a long term stability up to 100 days. A Monte Carlo simulation taking into account information obtained from the cosmic-ray test such as the NPE dependence on the incident particle position *etc.* was performed to estimate an on-line proton rejection efficiency. As a result, it is estimated that the developed water Čerenkov detector is able to achieve $> 90\%$ proton rejection efficiency keeping $> 95\%$ K^+ survival ratio in the whole S-2S momentum acceptance. The shown performance fulfills our requirements to perform the Ξ^- hypernuclear spectroscopy using the (K^-, K^+) reaction at J-PARC.

Acknowledgment

We would like to thank Aquarium Suiso-Kobo company for their technical support of the prototype design and construction. We would like to thank Tohoku ELPH (ELPH experiment #2783) and J-PARC for providing us opportunities of test experiments using beams. This work was supported by JSPS KAKENHI Grant Numbers 23000003, 13J01075.

References

- [1] Proposal at J-PARC, T. Nagae *et al.*,
P05: Spectroscopic Study of Ξ -Hypernucleus $^{12}_{\Xi}\text{B}$, via the $^{12}\text{C}(K^-, K^+)$
Reaction, http://j-parc.jp/researcher/Hadron/en/Proposal_e.html
- [2] T. Hasegawa *et al.*, *Nuclear Instruments and Methods in Physics Research A* **342**, 383-388 (1994).
- [3] T. Fukuda *et al.*, *Nuclear Instruments and Methods in Physics Research A* **361**, 485-496 (1995).
- [4] T. Gogami *et al.*, *Nuclear Instruments and Methods in Physics Research A* **729**, 816-824 (2013).
- [5] K. Nakamura *et al.*, *Journal of Physics G* **37**, 075021 (2010).
- [6] S. Agostinelli *et al.*, *Nuclear Instruments and Methods in Physics Research A* **506**, 250-303 (2003).
- [7] R. Ota, *Master's thesis, Osaka University, Osaka, Japan*, 2013.
- [8] Y. Ichikawa, *Ph.D. thesis, Kyoto University, Kyoto, Japan*, 2015.
- [9] T. Ishikawa *et al.*, *Nuclear Instruments and Methods in Physics Research A* **622**, 1-10 (2010).
- [10] T. Ishikawa *et al.*, *Nuclear Instruments and Methods in Physics Research A* **694**, 348-360 (2012).
- [11] E. H. Bellamy *et al.*, *Nuclear Instruments and Methods in Physics Research A* **339**, 468-476 (1994).
- [12] G.M. Hale and M.R. Querry, *Appl. Opt.*, **12**, 555-563 (1973).
- [13] R.M. Pope and E.S. Fry, *Appl. Opt.*, **36**, 8710-872 (1997).
- [14] T.I. Quickenden and J.A. Irvin, *Chem. Phys.*, **72**, 4416-4428 (1990).
- [15] G. Finocchiaro *et al.*, *Proceedings of Technology and Instrumentation in Particle Physics 2014* (2014).
- [16] Hamamatsu Photonics, <http://www.hamamatsu.com/jp/en/index.html>

[17] COBHAM, <http://www.cobham.com/>